Predicting the UHE photon flux from GZK-interactions of hadronic cosmic rays using CRPropa 3

Master Thesis
to obtain the academic degree
Master of Science
(M.Sc.)

University of Siegen

Naturwissenschaftlich
Technische Fakultät

Department of Physics

submitted by
Anna Bobrikova

October 2020

Abstract

Measurements of the ultra high energy cosmic rays (UHECR) spectrum at the ground level taken by the Pierre Auger Observatory indicate a suppression in the spectrum at about 50 EeV, the so-called cut-off. The origin of this suppression is still unclear. One possible explanation could be the so-called Greisen-Zatsepin-Kuzmin (GZK) process, in which ultra high energy protons interact with the photons of the cosmic microwave background and lose energy. Indirect evidence for the GZK-process could be provided by the search for UHE photons produced in such an interaction.

Although a possible photon signal could yet not be identified among the cosmic ray flux, upper limits on ultra high energy (UHE) photon flux have been derived from the experimental data. The low energy enhancements of the Pierre Auger Observatory allow search for photons with energies above 2×10^{17} eV.

In order to interpret the upper limits on the flux of the UHE photons derived from the experimental data, theoretical predictions are needed. Predictions of the photon flux above 1 EeV as expected from the propagation, in which GZK-process is included, have been derived in the past.

In the current thesis new predictions of the photon flux above 0.1 EeV are derived for both pure proton and mixed compositions of the initial cosmic rays, with latest results regarding the composition of CRs and the interstellar medium taken into account. For both pure proton and mixed compositions the predictions stay below the upper limits on the UHE photon flux at Earth derived from the experimental data. Main uncertainties on the predictions are coming from not yet full understanding of the UHECR sources and their features. Also, a step in the direction of estimating the impact of the sources emitting UHE photons into the UHE photon flux at the Pierre Auger Observatory is taken.

Contents

1 Introduction **1**

2 Cosmic Rays **3**
2.1 Energy spectrum and mass composition of cosmic rays 3
2.2 Origin of cosmic rays 5
2.3 Propagation of cosmic rays 10
2.3.1 Magnetic Fields 10
2.3.2 Interactions 12
2.4 Pierre Auger Observatory 15
2.5 Photons among the cosmic rays 17

3 CRPropa 3 **18**
3.1 Basic principle of operation 18
3.2 General Capabilities 19
3.3 Modification used 21

4 Pure proton cosmic rays propagation **23**
4.1 Discrete distances and discrete energies 23
4.2 Parameters study 26
4.3 Realistic scenarios 35

5 Heavy nuclei cosmic rays propagation **37**
5.1 Pure heavy nuclei cosmic ray propagation 37
5.2 Mixed cosmic ray propagation 39
5.2.1 Combined fit of the spectrum and composition data 39
5.2.2 Parameters study 41
5.2.3 Results 43

6 Photon cosmic rays **46**
6.1 Attenuation length of the UHE photons 46
6.2 Effective attenuation length 48

7 Summary and outlook **52**

1 Introduction

Astroparticle physics has plenty of unsettled questions. Hints that could help answer many of these questions could be obtained from the observation of cosmic rays (CR), ionizing radiation that reaches the atmosphere of Earth from outer space. For instance, questions of the acceleration mechanisms for ultra high energy cosmic rays (UHECR) and their chemical composition are the open ones, however, clues and indirect evidences could be obtained from the measurements of the air showers produced by cosmic ray particles in the atmosphere.

Cosmic rays mostly consist of the nuclei of atoms, yet there are also electrons. A considerable fraction of the hadronic part of the cosmic rays are protons, but heavier nuclei appear there as well. Cosmic ray particles have very high energies, as they travel with relativistic velocities. There are several hypotheses concerning the sources of the cosmic rays, but testing these hypotheses proves challenging, especially for the ultra high energy cosmic rays (UHECR) in EeV range, as sources of these particles are believed to be located outside of our galaxy.

Measurements of the cosmic rays started with balloons drifting in the atmosphere. Currently, there are two main types of the experiments developed to study cosmic rays: satellite-based experiments that detect cosmic rays on top of the Earth's atmosphere and ground-based experiments that operate on the surface of Earth. High-flying balloons and underground detectors are also of use. For ultra high energy cosmic rays, the most efficient way to observe them is to measure them indirectly by observing the air showers that these UHECR produce in the atmosphere. The Pierre Auger Observatory [1] is currently the largest experiment focused on the air showers from the ultra high energy cosmic rays with energies above 0.1 EeV.

Cosmic rays that we could observe on the top of the Earth's atmosphere had had to travel through space from their sources, interact with background light, and become deflected by the magnetic fields within and outside our galaxy. The task to understand the process of propagation of the cosmic rays from their sources towards Earth is a challenge, as many parameters of this propagation are unclear. There are different models and hypotheses concerning the structure of galactic and extragalactic magnetic fields, background light, and interactions in which particles of energies such high could participate in space.

Measurements of the UHECR spectrum at the ground level taken by the Pierre Auger Observatory indicate a suppression in the spectrum at about 50 EeV, the so-called cut-off. The origin of this suppression is still unclear. One possible explanation is the maximum acceleration energy of the sources, so particles with energies above 50 EeV simply could not be produced. Another explanation could be the interactions, specifically the so-called Greisen-Zatsepin-Kuzmin (GZK) [2] [3] process, in which ultra high energy proton interacts with the photons of the cosmic microwave background and lose energy. Indirect evidence for the GZK-process could be provided by the search for ultra high energy (UHE) photons that are produced in such an interaction. Although a possible photon signal could yet not be identified among the cosmic ray flux, upper limits on UHE photon flux have been derived from the experimental data [4], [5], [6]. The constantly growing amount of data collected at Pierre Auger Observatory along with refined analysis methods make it possible to improve the upper limits on the UHE photon flux. The low energy enhancements of the Pierre Auger Observatory (HEAT and SD 750 m array [1]) allow search for photons with energies above 2×10^{17} eV.

In order to interpret the upper limits on the flux of the UHE photons derived from the experimental data, theoretical predictions are needed. Predictions of the photon flux above 1 EeV as expected from the propagation of UHECR from their sources towards Earth, in which GZK-process is included, have been derived in the past [7], [8], [9]. The aim of this thesis is to study the propagation of cosmic ray hadrons and photons and derive updated predictions of the expected GZK photon flux including the latest results regarding the composition of CRs and the interstellar medium.

The thesis is structured as follows. In Chapter 2 a short overview of the cosmic rays and their known properties is presented. The energy spectrum of the cosmic rays and its features are introduced, possible sources for ultra high energy cosmic rays are discussed, and the main interactions of UHECR and their secondary particles are listed. Foundation and methodology of the study of photons among cosmic rays are given, and the Pierre Auger Observatory is introduced. CRPropa 3, a publicly available code for Monte Carlo simulations of the UHECR propagation, is introduced in Chapter 3. The main operation principles of the framework and the way the framowork is used in the thesis are presented as well.

The measurements of the Pierre Auger Observatory indicate a considerable fraction of protons among the CRs (at energies below EeV region), so the study of the pure proton UHECR and their propagation resulting in UHE photon flux predictions is shown in Chapter 4. For highest energies (above 1 EeV), however, it is expected for initial cosmic rays emitted from the sources to be of heavier mass composition (as discussed in [10], [11], [12]), so the predictions of UHE photon fluxes coming from initial cosmic rays of heavier and mixed mass composition are presented in Chapter 5. A step in the direction of estimating the impact of sources emitting UHE photons on the UHE photon flux at the Pierra Auger Observatory is taken in Chapter 6. Conclusions and outlook are discussed in Chapter 7.

2 Cosmic Rays

Cosmic rays are charged nuclei moving through space with the velocity close to speed of light. Every second, thousands of them hit every square meter of the Earth's atmosphere. Approximately 90% of the nuclei are protons, 9% are alpha particles, and 1% are heavier nuclei. The energy range of the cosmic rays is wide, from 1 GeV, which is close to their rest masses, to ultra-relativistic ones with energies above 100 EeV [13].

Victor Hess, one of the pioneers of the cosmic ray research, in 1912 took three Wulf electrometers on a hot air balloon and rose up to 5,000 meters to measure the ionisation of the atmosphere. He found out that ionisation increased significantly with the height of the measurement, and stated that "radiation of very high penetrating power enters from above into our atmosphere" [14]. In upcoming years, his discovery was confirmed [15], and, for many years, the procedure of sending self-operating electrometers on a balloon was the major way of studying this phenomenon. As the cosmic ray science evolved, new and far more efficient methods of detecting and distinguishing particles emerged, and, now, cosmic rays are measured on the surface of the Earth and deep below it, in the atmosphere, and even in outer space with many different types of detectors. The data collected from different experiments helps search for answers to the main questions about cosmic rays, such as sources of the cosmic rays and the mechanisms of their acceleration.

Within this chapter, features of the energy spectrum of cosmic rays are discussed in Sec. 2.1, the discussion of different possible sources of cosmic rays is given in Sec. 2.2, and details of the propagation of cosmic rays through space are described in Sec. 2.3. The Pierre Auger Observatory is introduced in Sec. 2.4. Lastly, ways to detect photons, non-charged messengers of the cosmic rays, and current upper limits on the flux of ultra high energy photons are discussed in Sec. 2.5.

2.1 Energy spectrum and mass composition of cosmic rays

Cosmic rays have been detected in the energy range from 1 GeV to above 10^{11} GeV, and within this energy range, the flux of the cosmic rays decreases by more than 30 orders of magnitude, from thousands of particles per second per square meter to less than one particle per square kilometer per century. It is from the variety of experiments we know that the dependency of the cosmic ray flux on energy can be described with a broken power law function with several features, see Fig. 2.1.1.

To understand the physics beyond this dependency, one must look into the energy density balance (following [17]). It could be noticed that energy density of the kinetic movement of matter ω_{T}, cosmic ray energy density ω_{C}, and magnetic field energy density ω_{G} are approximately equal in space volume near Earth:

$$\omega_{\mathrm{C}} \approx \omega_{\mathrm{G}} \approx H^2/8\pi \approx \omega_T = \rho u^2/2 = n k_{\mathrm{B}} T \approx 5 \times 10^{-6}\,\mathrm{eV/m^3}, \tag{2.1}$$

where H is magnetic field strength, ρ is the density of the matter, u is the velocity of the matter, n is a concentration, k_{B} is the Boltzmann constant, and T is the temperature of the matter.

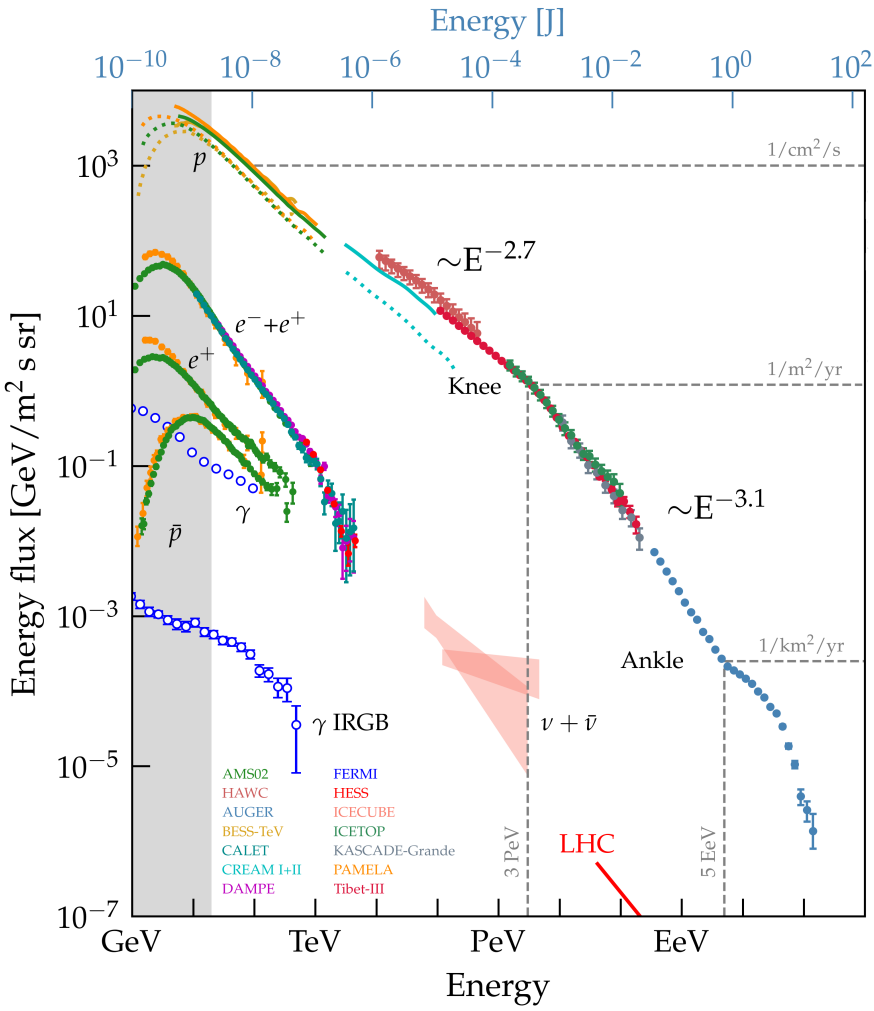

Figure 2.1.1: Differential energy spectrum of cosmic rays of energy above 10^9 eV multiplied by E^2 [16]. Together with the total CR spectrum, the spectra of specific particles (protons, photons, electrons etc) are shown. These spectra are the results of different cosmic ray experiments mentioned in the plot. Energies of the CR required to perform an interaction with the maximum centre-of-mass energy equal to the one of the Large Hadron Collider is shown at the energy scale.

This equation can be verbally interpreted as the equilibrium between the cosmic ray, magnetic field and kinetic energy densities. If the cosmic ray energy density in some arbitrary volume would start exceeding the magnetic field energy density, then magnetic field will not be able to restrain cosmic ray particles in this volume. Particles then will escape the volume, so the cosmic ray energy density will decrease and get back to equilibrium. Same holds for kinetic energy density. So the assumption that this equilibrium remains in any space volume could be made. One could write then for cosmic ray energy W_C and total energy W_{total}:

$$W_C = \frac{1}{3} W_{total} \tag{2.2}$$

Let ϵ be the energy of one average cosmic ray particle, and N_0 be the number of the particles. Then,

$$dW_{total} = d(3\epsilon N_0) = 3\epsilon dN_0 \tag{2.3}$$

where dN_0 is the change of the amount of the particles while they leave the volume. Further steps of the derivation are omitted here, yet it could be shown that from this assumption, the resulting differential spectrum could be derived:

$$dN_0(\epsilon) = A\epsilon^{-2.5}d\epsilon \tag{2.4}$$

where A is a constant. So the power law dependency with a spectral index of -2.5 occurs from very general assumption [17].

In Fig. 2.1.1, three main features of the spectrum could be noticed. The spectrum has a **knee** above 3 PeV, an **ankle** above 5 EeV, and a **cut-off** above 30 EeV. Between these features, the spectrum can be described as a power low dependency $E^{-\alpha}$ with slightly different spectral indices: $\alpha = 2.7$ below the knee and between the ankle and the cutoff, and $\alpha = 3.1$ between the knee and the ankle [18]. The data received at Kascade-Grande experiment shows another feature, the 2nd knee at about 80 PeV [19].

Physics behind these features are unclear, yet there are several possible explanations. For the **1st knee** a possible reason could be that some of the sources within the galaxy have their maximum acceleration energy at this energy range, so fewer particles are produced and hence observed for energies above the 1st knee (e.g., some types of the supernova remnants have their maximum energy limit at about 1 PeV). **2nd knee** could correspond to the transition from lighter to heavier initial hadrons: as, in general, the lightest hadrons (protons) have higher energy per nucleon, and almost all heavy nuclei decay into lighter ones, the decrease of the spectrum with energies above the 2nd knee could be expected. The **ankle** is understood as the place of a smooth transition from galactic to extragalactic cosmic rays [20]. It could be because particles with energies higher than 1 EeV are expected to have their gyroradii being larger than the size of our galaxy [13]. With this change of origin of the UHECR comes the change of the spectrum's behaviour. Finally, the **cut-off** could be an evidence for either lack of sources with higher energies of emitted particles or the GZK process (UHE proton interacting with the photons of the cosmic microwave background, see Sec. 2.3.2).

Concerning the chemical composition (mass composition) of the cosmic rays, all stable nuclei from the periodic table could be observed in the cosmic ray spectrum [21]. Some of the fluxes of different components of the cosmic rays are shown in Fig. 2.1.2.

2.2 Origin of cosmic rays

The sources of the cosmic rays are not yet fully clarified. It is known so far that the Sun as a source does not play a major role in the cosmic ray spectrum observed on Earth, as only a few particles produced during the solar eruptions could contribute to the cosmic ray spectrum at energies $E < 2 \times 10^{10}$ eV [29]. As was discussed above, the ankle of the cosmic ray spectrum is believed to be the range at which the flux of the cosmic rays of galactic origin (below the ankle) is smoothly exceeded by the flux of the cosmic rays of extragalactic origin. Cosmic rays of energies below 1 EeV are believed to be mostly of galactic origin, and the ones with higher energies are coming from outside of our galaxy.

There are different models for the processes of creation of the UHECR. Non-acceleration models consider processes of decay or annihilation of primordial relics such as topological defects or

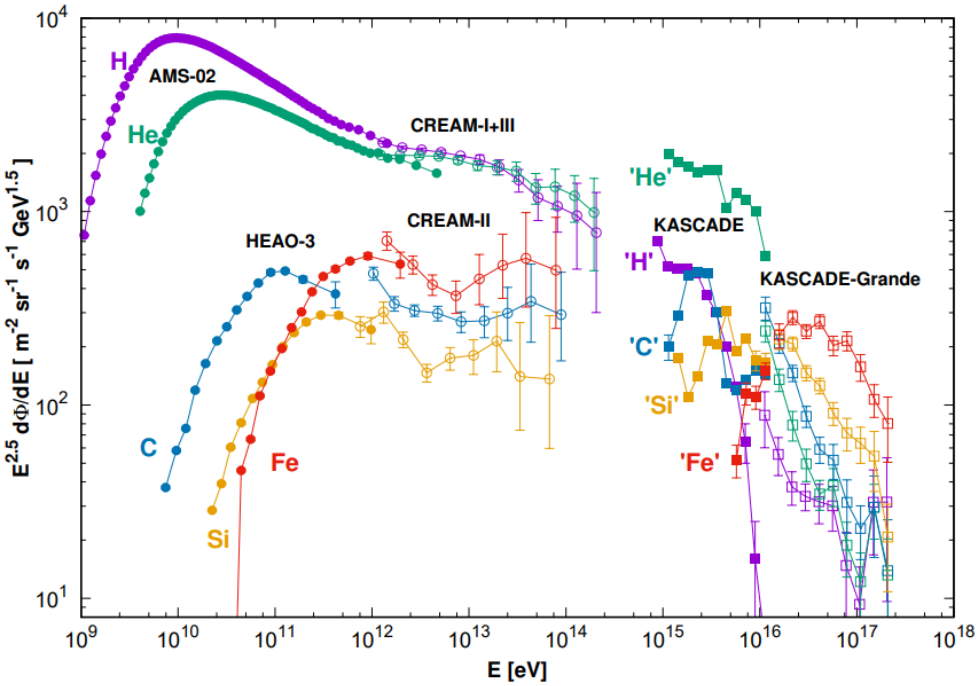

Figure 2.1.2: Spectra of different components of the cosmic rays [21]. Data by AMS-02 in the International Space Station for H [22] and He [23] fluxes, by HEAO-3 satellite for C, Si and Fe fluxes [24], by balloon flights CREAM-I and CREAM-III for H and He fluxes [25], by balloon flight CREAM-II for C, Si and Fe [26]. Results for higher energies are from KASCADE [27] and KASCADE-Grande [28]. Elements here are grouped to 'mass ranges' labeled by a representative element.

super heavy dark matter to be responsible for the creation of the UHECR [30]. Acceleration models require sources in which cosmic ray particles could be accelerated to ultra-high energies. Mechanisms of this acceleration could be divided into two classes: diffusive and inductive.

Diffusive shock acceleration (stochastic acceleration) is a process in which particles are moving around inside the accelerator and eventually receiving energy while interacting with inner structure of the accelerator itself [31], and this happens again and again until the particle gains enough energy to escape the accelerator. Typical examples of diffusive acceleration are first and second order Fermi accelerations [32].

Second order Fermi acceleration is a process in which a particle gets inside the magnetised plasma cloud and diffuses by elastic non-collisional "scattering" on the irregularities in the magnetic field [13]. If the shock front is involved, a particle goes through the front into the cloud, get deflected by the irregularities in the magnetic field (and probably participates in the 2nd order Fermi acceleration), and then goes back through the front, it gains even more energy while being accelerated by the shock front itself. This acceleration with the shock wave is called 1st order Fermi acceleration. The processes are named so, as the energy gained in one encounter is proportional to β in 1st order Fermi acceleration and to β^2 in 2nd order Fermi acceleration, where $\beta = v/c$, ratio of the velocity of the cloud to the speed of light. One encounter of each of the processes is shown in Fig. 2.2.1.

Inductive acceleration (one shot acceleration), on the other hand, is a mechanism in which parti-

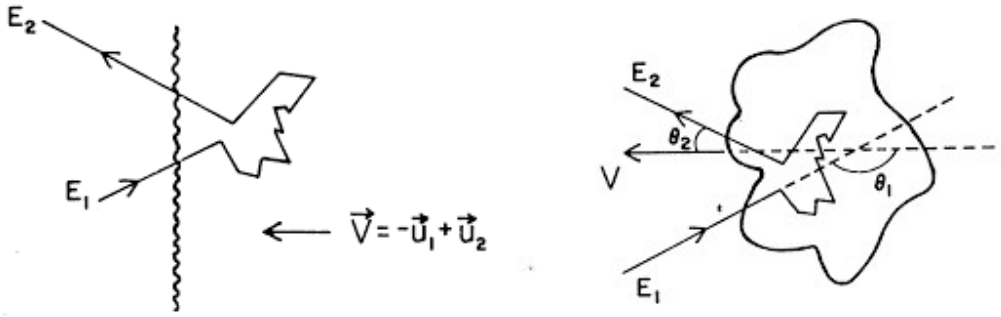

Figure 2.2.1: Illustration of the Fermi acceleration mechanisms [13]. *Left:* Acceleration at a plane shock front, 1st order Fermi acceleration. *Right:* Acceleration by a moving, partially ionized gas cloud, 2nd order Fermi acceleration.

cles are directly (in one shot) accelerated by the electric fields arising from the alteration of the magnetic field. These accelerators, at their turn, could be divided into ones with synchrotron-dominated losses (e.g. active galactic nuclei) and ones with curvature-dominated losses (neutron stars and black holes). Curvature radiation is the one coming from a particle sliding along a curved magnetic field line. Synchrotron radiation is the one coming from a particle gyrating around a straight magnetic field line. Whether the former or the latter dominates while charged particles move on curved trajectories depends on the magnetic field, radius of the curvature, pitch angle between the magnetic field and the velocity of the particle and the Lorentz factor of the particle [33]. Acceleration mechanisms are discussed in more details in [34].

While searching for the possible sources of the cosmic rays, one must consider several restrictions on their properties. Geometric criterion states that the size of the accelerators should exceed the space needed for a particle to accelerate. The restriction on power of the source states that the accelerator needs to be able to provide the particles with enough energy, with energy losses due to radiation, curvature and interactions being taken into account. Finally, the observational criterion states that the the combination of all sources should be able to provide the energy and distribution of the observed cosmic ray flux, with energy spectra of secondary photons and neutrinos being taken into account [35].

Both geometrical restriction and radiation losses are considered in the Hillas criterion: the Larmor radius of the accelerated particle should not exceed the size of the accelerator. In Fig. 2.2.2 possible source classes are shown with respect to their comoving size and magnetic field strength. Solid and dashed lines represent the Hillas criterion: the source needs to be above the line in order to fulfill this condition.

Supernova remnants (SNR) are believed to be responsible for the production of the bulk of galactic cosmic rays. The idea was proposed in [37], where it was mentioned that even 5-10 % of SNR kinetic energy being converted to cosmic rays would give enough energy to cover all the observed galactic CRs. Data from Fermi Space Telescope were interpreted [38] as the evidence for SNR being the main source of the cosmic rays. As the expansion velocity of the SNR is much higher than the sound velocity of the interstellar medium, the shock ahead of the expanding SNR is formed [18]. SNR is an example of an accelerator with diffusive shock accelerating mechanism (1st order Fermi acceleration).

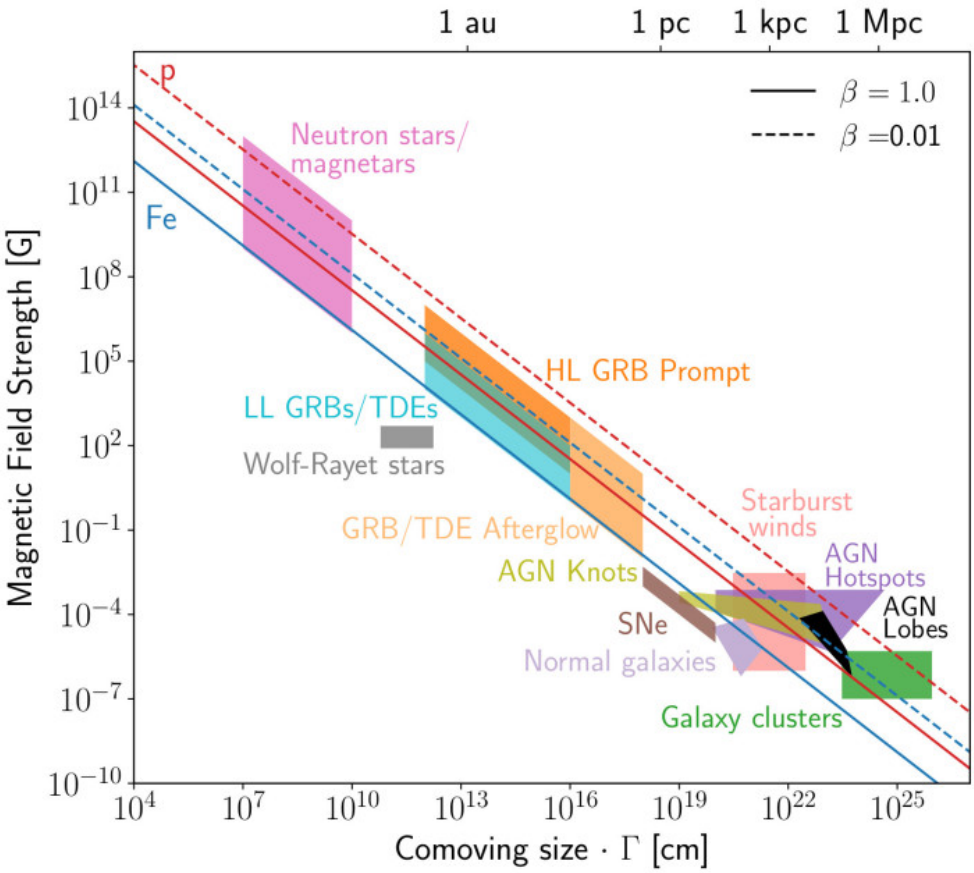

Figure 2.2.2: Hillas plot, version from [36], originally from [34]. Characterization of astrophysical objects with respect to size and magnetic field strength. In order to be able to accelerate named particles to noted energies, the object should be above the corresponding line. β here refers to the velocity of the shock front of the source responsible for the acceleration of the UHECR particles.

When it comes to ultra high energy (extragalactic) cosmic rays, there are several possible types of the sources.

Pulsars and magnetars are rotating neutron stars hosting the strongest magnetic fields known to us in the universe [39]. Magnetars have magnetic field up to 10^{14} G, and pulsars have the magnetic field in a range of $10^{11} - 10^{12}$ G. Pulsars and magnetars have what is required to be the source of the UHECR: with their rotating magnetosphere on the first stage of their evolution, they are capable of transferring enough energy to accelerate heavy cosmic ray particles (iron) to energies up to 10^{20} eV [40], then they lose their power and further on could produce CR particles with energies of a few EeV. The birth of a magnetar is also believed to be a possible source of primary UHECR particles with energies up to $10^{21} - 10^{22}$ eV, that would correspond to the particles of few times 10^{20} eV on the top of the Earth's atmosphere [41]. Detailed analysis of the pulsars as potential sources of the UHECRs is presented in [39].

Active galactic nucleus (AGN) is a small area at the center of a galaxy with extremely high electromagnetic (EM) luminosity (with broad band EM spectrum: from radio waves to gamma radiation). At the center of such a galaxy, there is a supermassive black hole which accretes

mass from the galaxy. It emits relativistic matter via two jets. Galaxies with an active nucleus are used to be divided into Seyfert galaxies, quasars, BL Lacertae objects, blazars and radio galaxies, while current theories of unification are to prove that these objects belong to the same astronomical class of objects, as they vary by the point of view, not by their structure, see Fig. 2.2.3 [42]. It is also stated that for a galaxy being active is not a permanent feature but a temporary state [43].

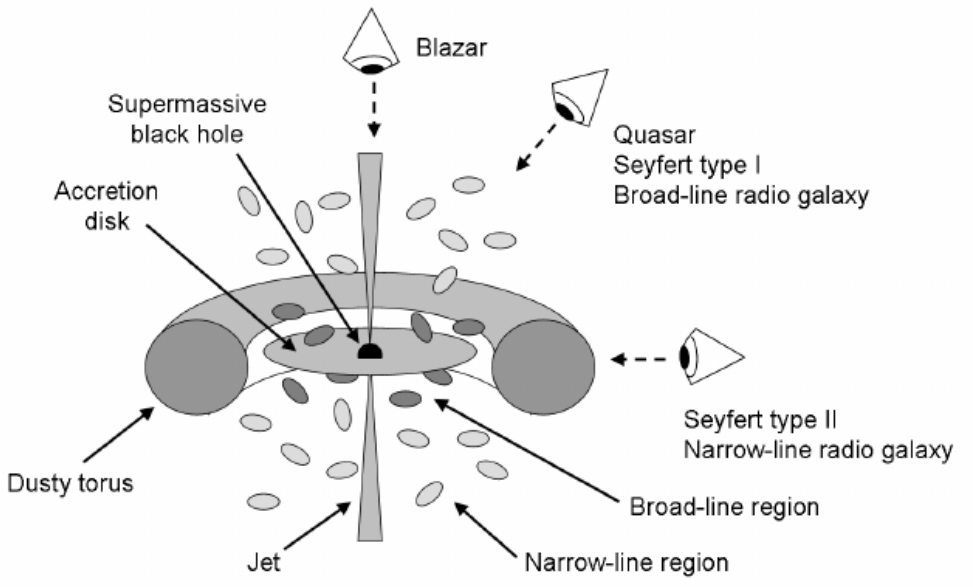

Figure 2.2.3: Unification of active galactic nuclei classes [42]. The object of presented structure is observed as ones of several different astronomical classes depending on the point of observation.

Star formation regions and starburst galaxies. In star-forming regions the molecular clouds collapse and form stars. These regions are not considered as possible UHECR sources [44], except for the starburst galaxies, galaxies with extremely high star formation rate. The galaxy transit to starburst state when collapsing or closely moving by another galaxy. In this case, the conditions within the galaxies are changing: the star-formation rate increases, i.e., the whole amount of gas that the galaxies could possibly transform into stars is used in a short period of time (comparing to the age of the galaxies themselves) [45]. Here, the particles could be first accelerated by supernova remnants, but then avoid photo-disintegration, and, instead, be reaccelerated at the terminal shock. The shock, in this case, is the result of the so-called "galactic superwind", the collective effect of supernovas and massive star winds coming from the starburst galaxy [46].

Gamma ray bursts are explosions of extremely high energies. Typically, these events last for several seconds, yet it could be several ms or hours. Gamma ray bursts happen in distant galaxies. There are currently two main progenitor models: the "collapsal" one (fast rotating core of the supermassive star collapses and transforms into a neutron star or a black hole) and the "merger" one (two compact objects, e.g. neutron stars, spiral slowly toward one another, release gravitational energy until the tidal forces rip the progenitors apart and the system collapses into

a single compact object). In both scenarios, the infalling material forms a dense accretion disk that ejects two relativistic jets [47].

The sources of different types are non-uniformly distributed within the universe. According to [34], a possible explanation is the existence of the galaxy clusters (and superclusters), large groups of galaxies (or of galaxy clusters). Galaxies in the cluster are bound together by gravity. Galaxies make up 1% of total mass of the cluster, and 9% are of intergalactic gas; the remaining mass is assumed to be dark matter. The tendency of the galaxies to form groups leads to non-uniform distribution of the sources of the UHECR in space.

Cosmological evolution of the sources $d\rho/dt$, the change of the source emissivity and space density with redshift, is observed for many astronomical populations [44].

- Star formation rate (SFR), a general indicator of the matter density in the Universe, has been measured for different objects, and there are currently several SFR traces and, consequently, several models of the SFR-type source evolution. In Fig. 2.2.4 two of them described in [48] and [49] are shown. As only redshift z<1 area is of interest for the propagation simulated in current thesis, the source evolution for SFR could be sufficiently described with $(1 + z)^m$, m=3.4.

- The evolution of gamma ray bursts with redshift is described in [50]. In Fig. 2.2.4 two models that are close to SFR evolution up to $z \approx 4$ are shown, with the emissivity evolving as $(1 + 8z)/[1 + (z/3)^{1.3}]$ and as $(1 + 11z)/[1 + (z/3)^{0.5}]$ for GRB1 and GRB2 respectively [51].

- Active galactic nucleus is a wide class of astronomical objects with different evolutions. In Fig. 2.2.4, the source evolution for a Faranoff-Riley II type galaxy is shown [52]. For small redshift z<1, this one can be approximated with $(1 + z)^{5.5}$.

2.3 Propagation of cosmic rays

After being emitted from the sources, cosmic ray particles move through space where they get deflected by magnetic fields, emit synchrotron radiation, and interact with low-energy cosmic background radiation.

2.3.1 Magnetic Fields

Charged cosmic ray particles are deflected in a magnetic field with relativistic Lorentz force, proportional to the charge and velocity of the particle and the strengths of the magnetic field in a direction perpendicular to the velocity. Magnetic field effect does not directly depend on the mass of the particle and is fully dependent on the rigidity, the ratio of the particle's momentum to its charge. The only effect dependent on the mass of the particle is the synchrotron emission loss, yet it is negligibly small compared to other effects. General review on astrophysical magnetic fields is given in [53].

The magnetic field of our galaxy is not fully understood yet. It is usually described as a combi-

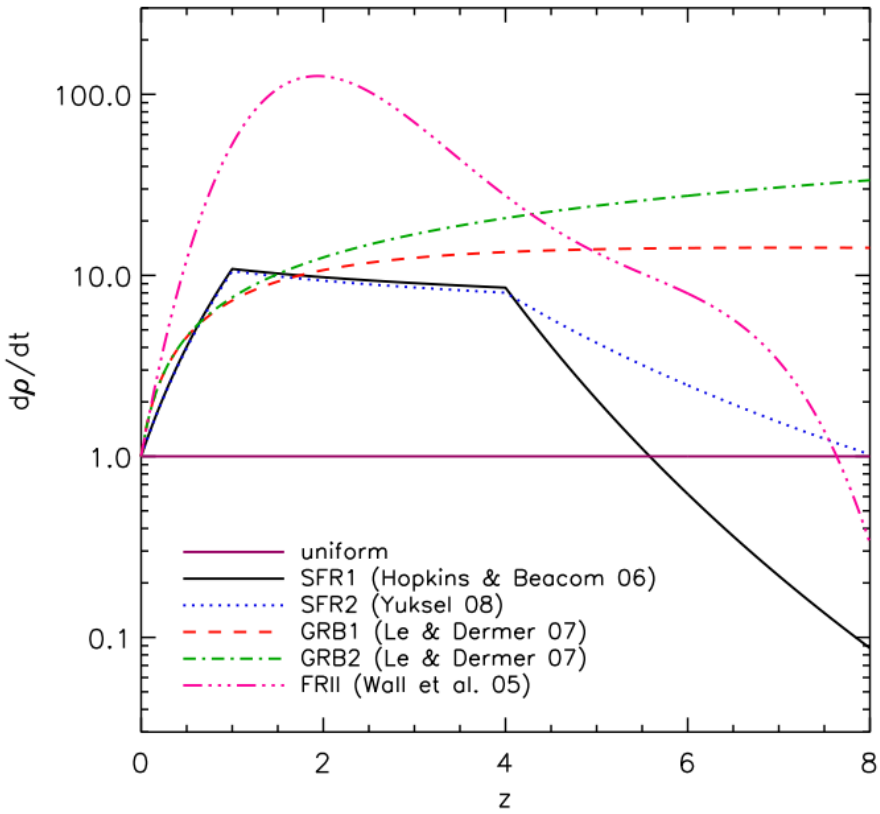

Figure 2.2.4: Theoretical predictions of the source emissivity evolution with redshift, normalized to unity at z = 0 [51]. The small redshift (z<1) range is of interest for the current thesis.

nation of a strong regular magnetic field in the plane of the galaxy and small random turbulent fields. For the regular component of the magnetic field within the galactic plane, several configurations are derived, mostly based on rotational symmetry around the galactic center, and on mirror symmetry with respect to the galactic plane [54]. The strength of the magnetic field within the galactic plane is measured and can be described with function $e^{-R/8.5}$ for R, radius from galactic center, being larger than 3 kpc. Closer to the center of the galaxy, the field is hard to measure, yet there are evidences of field perpendicular to the plane near the galaxy center. Field outside the galaxy plane is an open question to this day [18].

There are two main models of the galactic magnetic field of the Milky Way. Pshirkov GMF model [55] was created from full-sky rotating measurements and consists of two parts: symmetric spiral disk and anti-symmetric halo. JF2012 [56], the most sophisticated and modern model, is a result of thousands of Faraday rotation measurements. It combines a disk field and a huge out-of-plane component.

Extragalactic magnetic field (EGMF) models are usually constructed as a combination of a grid with a structured low magnetic field and arbitrarily spread, non-regular components representing organised magnetic fields of astrophysical systems such as galaxy superclusters. Out of all the models of EGMF, two are chosen to be used in the thesis: the one with a rather weak magnetic field from Dolag et al [57] and a stronger one from Miniati et al [58].

2.3.2 Interactions

While propagating through space, nuclei collide with background photons in different photo-nuclei interaction scenarios and emit secondary particles, which, depending on their type, have their own way of interacting with background photons.

Photon background can be separated in parts by origin and energy range. The cosmic microwave background (CMB) and its evolution with redshift are well-known and precisely described, yet for other backgrounds, such as the infrared background light (IRB) and the universal radio background (URB), several models exist. CMB is known to have a temperature of 2.7 K, corresponding to a frequency of 160 GHz following a thermal distribution, and the average photon of this background has energy of 10^{-3} eV. IRB has higher average energy (10^{-2} eV), which means one order of magnitude higher frequency and temperature. URB has much lower average energy (10^{-9} eV), so the temperature and frequency are six orders of magnitude smaller. Energy spectra of these three components of the photon background radiation is shown in Fig. 2.3.1.

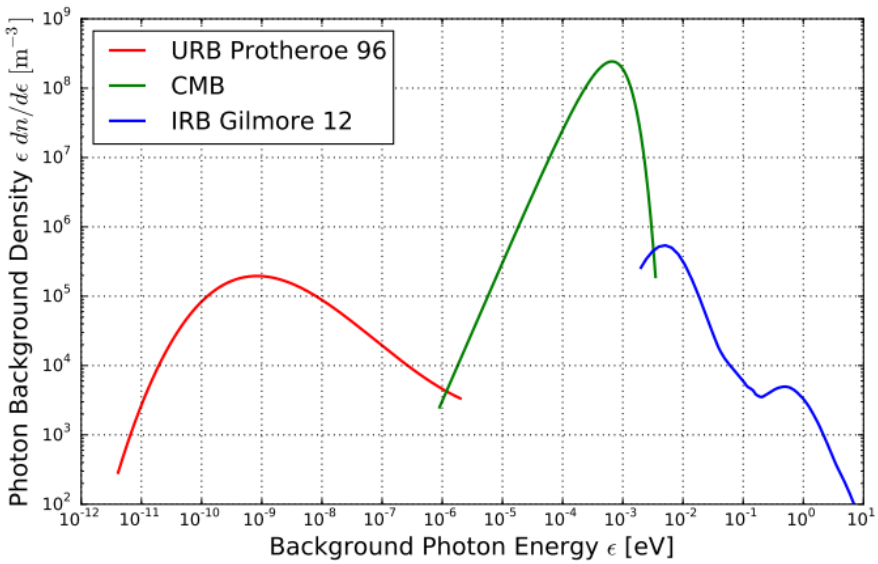

Figure 2.3.1: Energy spectrum of the photon background light with actual models from the CRPropa 3 [59]. Red line corresponds to URB [60], green line — to CMB, blue line — to IRB [61].

.

Photo-pion production via Greisen-Zatsepin-Kuzmin process is the dominant interaction between UHECR and photon background. High energy protons interact with photons of the background via the Δ resonance, which subsequently decays into nuclei and a pion.

$$\begin{aligned} p + \gamma_{bg} &\rightarrow \Delta^+ \rightarrow p + \pi^0, \\ p + \gamma_{bg} &\rightarrow \Delta^+ \rightarrow n + \pi^+ \end{aligned} \tag{2.5}$$

This interaction is named Greisen-Zatsepin-Kuzmin (GZK) process [2], [3]. It is stated that UHE protons with energies $E > 5 \times 10^{19}$ eV have a mean free path of only few tens of megaparsecs and effectively lose energy via such an interaction. The significant decrease of the characteristic time of this interaction of a proton can be noticed in Fig. 2.3.2, a. This would lead to the cut-off in the CR spectrum, see Fig. 2.3.2, b. The solid line corresponds to the CMB background light.

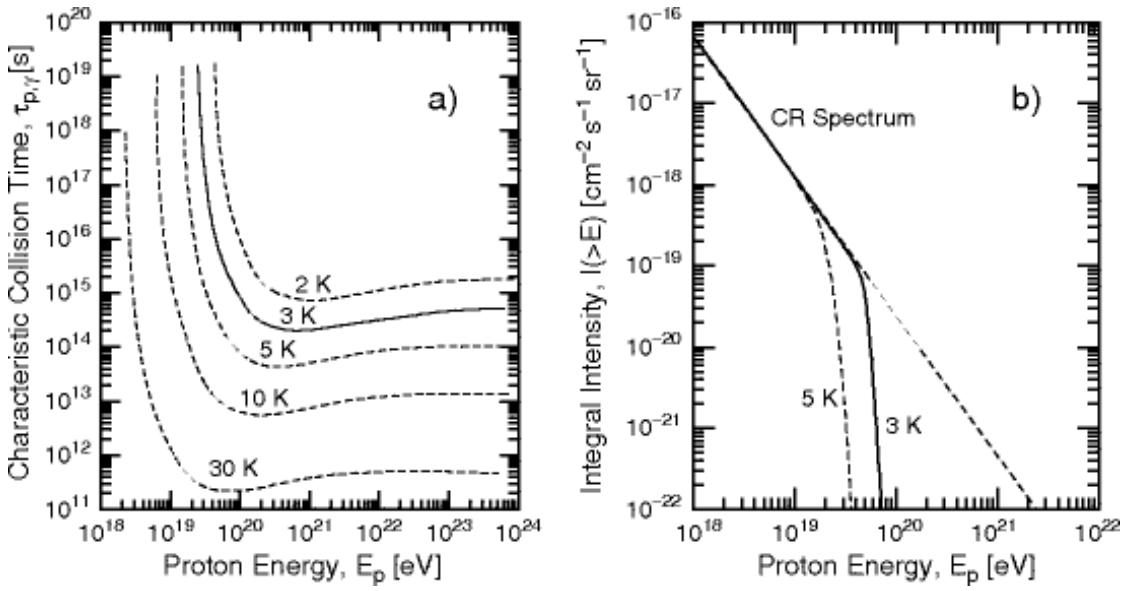

Figure 2.3.2: *Left:* Characteristic time of photo-pion production for different temperatures of the background radiation originally from [3], reconstructed in [62]. Solid line corresponds to the cosmic microwave background. Line with 30K close to infrared background light, and the universal radio background line would be higher than the one with 2K. *Right:* Integral intensity of the CR flux and the impact of the GZK process [62]. Solid line corresponds to the cosmic microwave background.

One could possibly think about heavier nuclei as the source to overcome the GZK-cutoff. However, for heavier nuclei, the dominant energy-loss process is **photo-disintegration**. The threshold energy for this process is two orders of magnitude lower than the one for photo-pion production [2]. Photo-disintegration happens as follows: an atomic nucleus absorbs a background photon, becomes excited, and immediately decays by emitting one or several particles such as proton, neutron or alpha particle. Photo-disintegration path of Fe nucleus is shown in Fig. 2.3.3. Total mean free path for various nuclei is shown in Fig. 2.3.4. The regions where different photon background fields play a dominant role in the process of photo-disintegration are marked in the plot.

Nuclear decay is the process which happens to radioactive isotopes. Unstable isotopes decay into stable ones and emit alpha particles (alpha decay), electrons, positrons and neutrinos (beta-decay), or photons (gamma-decay).

Elastic scattering is another photo-hadronic interaction. Photons of the background elastically scatter on UHE nuclei and gain energy. Interaction lengths of elastic scattering is one order of magnitude bigger than the one for photo-disintegration is. Therefore, this process is dominated by the latter.

Another process responsible for energy loss of UHECR is **electron pair production**. When UHE nucleus comes near the background photon of large enough energies, the energy of a photon is translated into creation of an electron-positron pair. The threshold for this process is $\approx 5 \times 10^{17}$ eV for protons. Near the threshold, pair production dominates over other photo-nuclear interactions. Comparison of the energy losses due to photo-pion production and electron pair production for protons is given in Fig. 2.3.5.

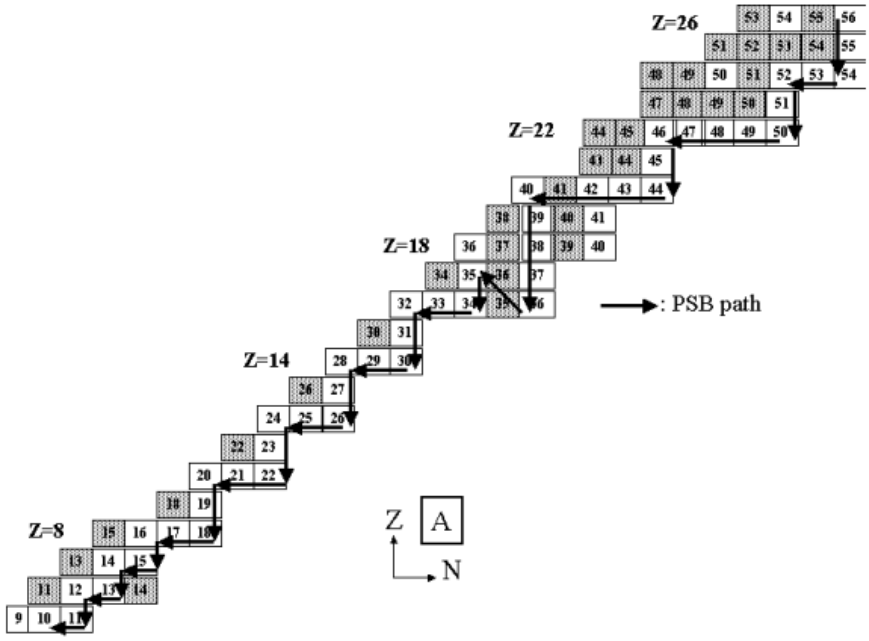

Figure 2.3.3: Nuclei involved in the photo-disintegration process of ^{56}Fe nuclei for $\gamma = 2.10^{10}$ [63]. Unstable nuclei are in shaded squares, and the photo-disintegration path is indicated by the arrows. The mass number of each nucleus is written in the corresponding square.

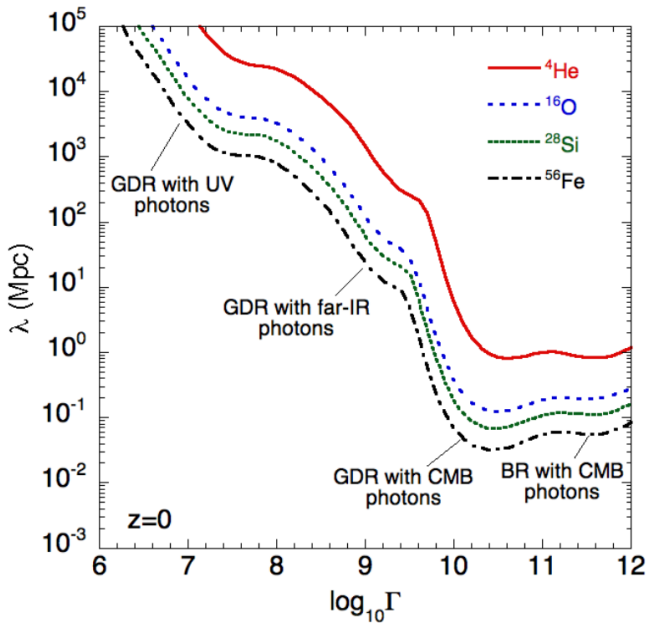

Figure 2.3.4: Total photo-disintegration mean free path for various nuclei at z = 0 as a function of the Lorentz factor Γ [64]. GDR stands for giant dipole resonance, BR stands for baryonic resonance.

These are the main processes happening to the UHE nuclei and their hadronic secondary particles. Total energy loss length for $^{14}_{7}N$ and $^{56}_{26}Fe$ nuclei and contributions of main photo-nuclear processes are shown in Fig. 2.3.6.

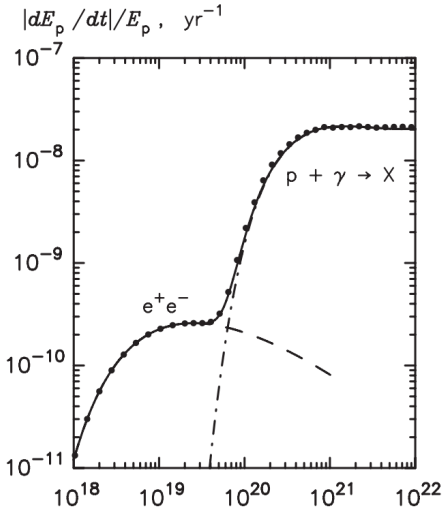

Figure 2.3.5: The average energy loss rates of protons while interacting with CMB radiation of temperature 2.7 K due to electron pair production and photo-pion production [65].

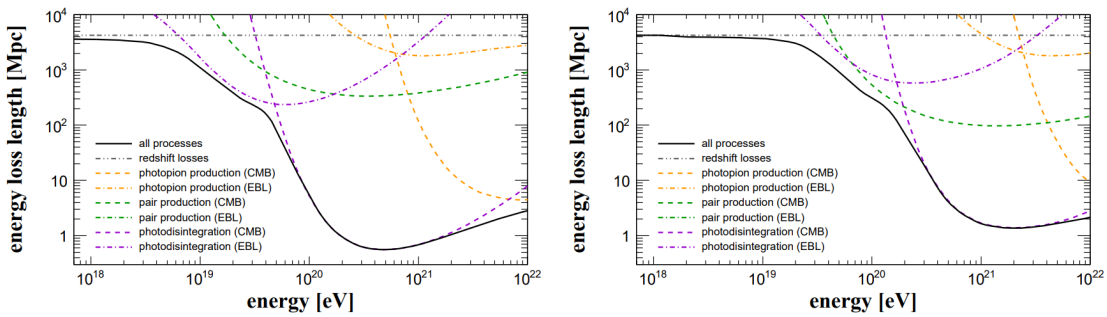

Figure 2.3.6: Energy loss length for N (left) and Fe (right) at z = 0 [66]. Interaction with cosmic microwave background (CMB) and extragalactic background light (EBL) are shown.

Electrons, positrons and photons produced in these interactions, however, have further ways to collide with photon background and interact with magnetic fields. For electrons, dominant processes are **inverse Compton scattering** ($e^{\pm} + \gamma_{bg} \rightarrow e^{\pm} + \gamma$) and **triplet pair production** ($e^{\pm} + \gamma_{bg} \rightarrow e^{\pm} + e^{+} + e^{-}$). For photons there are **pair production** ($\gamma + \gamma_{bg} \rightarrow e^{+} + e^{-}$) and **double pair production** ($\gamma + \gamma_{bg} \rightarrow 2(e^{+} + e^{-})$).

In general, all charged particles emit **synchrotron radiation** when deflected in a magnetic field. UHE nuclei, due to their rigidity, are barely deflected by magnetic fields. However, it is an important process for secondary electrons. Synchrotron radiation is also a channel of photon production, but within energy range considered in this thesis those photons are negligible due to small energies.

2.4 Pierre Auger Observatory

As the flux of the UHE particles is low, it is only possible to indirectly detect them with measuring air showers they cause once reaching the top of the Earth's atmosphere. To that end,

experiments with huge exposure are operated, Pierre Auger Observatory being the largest of them.

At the surface, 1660 water-Cherenkov detectors are spread within more than 3000 square km area with a spacing of 1500 meters. Water-Cherenkov detectors measure the profile of an air shower on the surface of the Earth and are called surface detectors (SD). When the air shower reaches the Earth's surface, it is possible, from the intensity of the Cherenkov light in the water tank, to understand, where the "axis" of the air shower is, and to detect the photon density as a function of the distance from the shower axis, so-called lateral distribution. Then, one could estimate both energy of the CR particle that produced the shower at the top of the atmosphere and the mass composition of the CR from this distribution. An example of the measurement performed by surface detector is shown in Fig. 2.4.1.

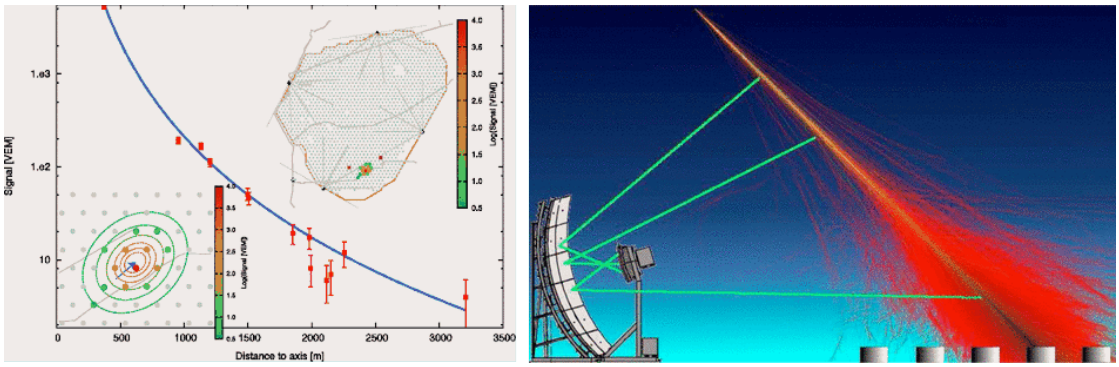

Figure 2.4.1: *Left:* Example of the detection of the air shower using surface detector. The whole Pierre Auger Observatory is shown in the top-right corner, the area of the detection is shown in more details in the bottom-left corner. The curve is the lateral distribution function, see text. *Right:* Sketch of the detection performed by the fluorescence detector. Pictures from the Pierre Auger Collaboration.

This array of surface detectors is surrounded with 27 fluorescence telescopes, overlooking the area from four sites and measuring the longitudinal shower development. Fluorescence detectors (FD) work as follows: the electromagnetic component of the air shower emits isotropic fluorescence light, which is then collected on a large mirror and detected by a camera composed of photomultipliers. With this technique, the atmosphere is used as a calorimeter, so the energy of the CR particle at the top of the atmosphere could be derived from the observations. Furthermore, an atmospheric depths of the shower maximum $X_{\max}$ is a direct observable in this measurement, and its distribution is known to be the most direct mass composition indicator. The sketch of the detection performed by a fluorescence detector is shown in Fig. 2.4.1 [1].

Smaller array of surface detectors called the SD 750 meters array (with SD being distributed with the spacing of 750 meters) and the High Elevation Auger Telecopes (HEAT), which are specifically inclined to measure showers above the field of view of other FDs (as the low energy air showers die faster in the atmosphere) is a setup created to measure air showers from the UHE particles of energies above 0.1 EeV [67].

2.5 Photons among the cosmic rays

Photons are secondary messengers of the creation and propagation of the UHECRs. Photons could be produced during the propagation of CR particles through space within the interactions of cosmic ray particles with the background radiation (mostly from the decay of previously produced neutral pions), or they could be created at the source of the CR particles by their interacting with the matter or magnetic fields surrounding the source itself. Also, the non-acceleration mechanisms of producing cosmic rays could lead to the creation of the UHE photons. Photons could, in turn, interact with the background radiation within the processes mentioned in Sec. 2.3.2.

Knowledge of the UHE photon flux may give clues and answers to many open questions of modern science. Photons are not deflected by magnetic field, and their physics is well-known from QED, so the UHE photon flux received on Earth could help in deriving the location of the points of creation of the UHE photons and give some clues about the nature of these processes.

UHE photons could also be the messengers of new physics. for instance, they could shed some light on non-acceleration models of UHECR production or confirm or refute the GZK effect. Search for UHE photons is highly motivated, yet, so far, there has been no photon measured with energies above 450 TeV [68].

With the data collected at Pierre Auger Observatory since 2004, it is possible to derive the upper limits on the UHE photon flux. Upper limits on the integral UHE photon flux at 95% confidence level (C.L.) are derived as a ratio:

$$\Phi_{UL}^{0.95}(E_\gamma > E_0) = \frac{N^{0.95}(E_\gamma > E_0)}{\mathscr{E}_\gamma(E_\gamma > E_0|E_\gamma^{-\Gamma})} \tag{2.6}$$

where $N^{0.95}$ stands for Feldman-Cousins upper limit at 95% C.L. assuming zero background, $\mathscr{E}_\gamma$ is the integrated Monte-Carlo predicted exposure above the energy threshold with initial power law spectrum $E^{-\Gamma}$ [69]. Slightly different statistical approaches are used in [4], [5] and [6]. Their results together with the limits from Pierre Auger Observatory are shown in Fig. 2.5.1.

Combined with the upper limits derived from the experimental data, the model predictions of the UHE photon flux are shown in Fig. 2.5.1. All three predictions extracted from [7] and [8] are based on the assumption that GZK process is the main production channel of the UHE photons. Differences between these predictions are due to different astrophysical scenarios used to describe the creation and propagation of the hadronic cosmic rays (protons or iron nuclei) from their sources towards Earth.

This thesis's aim is to give new model predictions for photon fluxes with energies above 0.1 EeV.

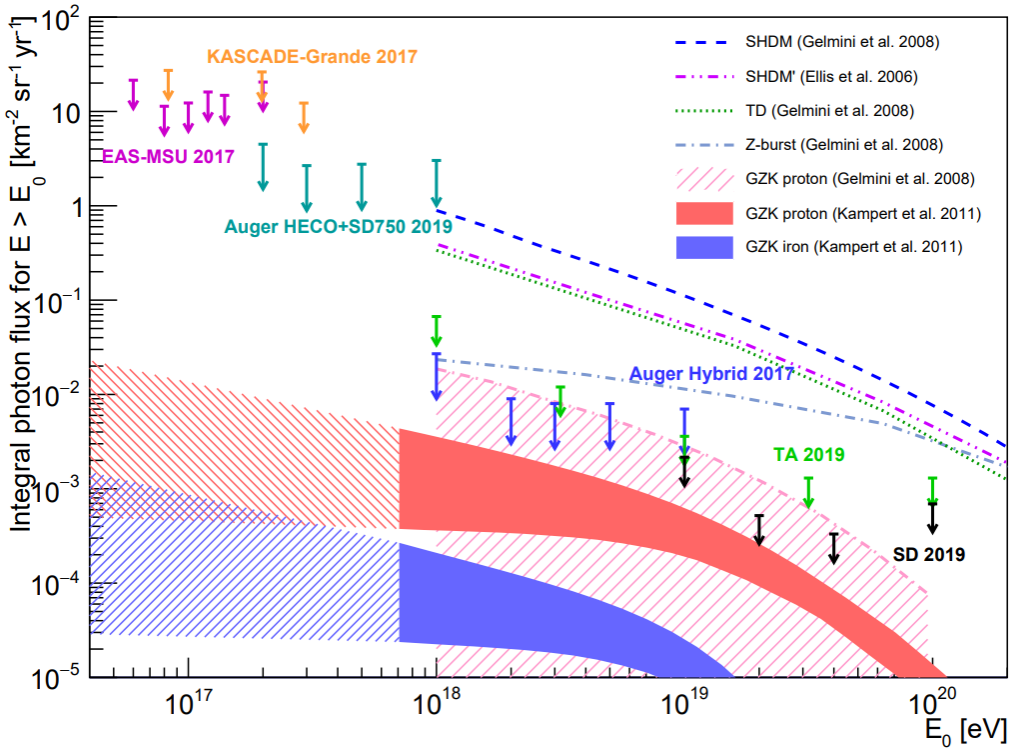

Figure 2.5.1: Photon flux limits at 95% C.L. for different analysis from the Pierre Auger Observatory [67], compared to model predictions and other experimental limits at 95% C.L. [5], as well as at 90% C.L. [4], [6]. Coloured and dashed areas correspond to model predictions of the UHE photon flux calculated in [7] and [8].

3 CRPropa 3

Simulation framework CRPropa 3 is a numerical tool developed to calculate different astrophysical predictions of cosmic ray propagation [70]. It includes combined knowledge of multiple aspects of cosmic ray sources, possible interactions, magnetic fields, photon backgrounds, and cosmological effects. CRPropa 3.1.5 is used in the current thesis.

Main structure of the framework is shortly described in Sec. 3.1. The general overview of the tool's capabilities is presented in Sec. 3.2. List of features used for current simulations is given in Sec. 3.3.

3.1 Basic principle of operation

CRPropa 3 is a modular tool adapted for multi-core calculations. Propagation of each particle (so-called candidate) is independent. Therefore, it is possible to process them in parallel. OpenMP is used to enable shared memory multiprocessing.

All the aspects of the simulations, from source parameters to observer properties, are separated into independent modules, which, in different combinations, form the scenario of the simulation,

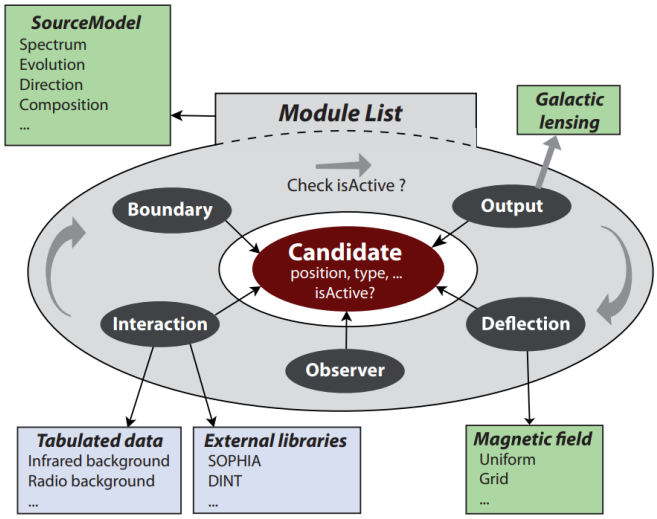

Figure 3.1.1: Schematic representation of the modular structure of CRPropa 3 [70].

see Fig. 3.1.1. Broad variety of modules is presented by creators of the tool, yet it is possible for the user to add his own modules if needed. Every combination of modules can be set as a propagation scenario, so CRPropa 3 is a useful tool to study impact of different features on the propagation.

The propagation process for each candidate starts with defining individual properties of the CR particle determined by the source features or directly by the user. At each step of the propagation, these properties are changed with respect to permanent processes (e.g. synchrotron radiation). Then, the probability for the particle to participate in any of stochastic interactions (e.g. photo-pion production) is calculated with respect to interaction length of each interaction for a particle with current properties. All the secondary particles produced in the interaction are, if required, added to the end of the queue of the particles to be propagated and, in turn, are treated as candidates themselves. Afterwards, another propagation step of variable size is taken. The propagation of the current candidate ends when it reaches the detector or fulfills a terminating condition (e.g. minimum energy limit or propagated distance), determined by the user. For each particle that reaches the detector, it is possible to extract various properties of this particle as a result of the propagation.

3.2 General Capabilities

CRPropa 3 has two propagation modes, 1D and 4D. In 1D simulation, particles are emitted and, then, propagated on a line towards the observer. The redshift is calculated in advance using the distance between the source and the observer. In 4D simulation, a full 3D-propagation is presented, and the redshift is counted as the fourth dimension.

All kinds of magnetic fields are supported in CRPropa 3. The user can define the magnetic field as a vector uniform field, as a periodic magnetic field grid, or as a random turbulent field. Any model of the magnetic field created by the user can be added to the simulation. For extragalactic propagation, models from [57] and [58] can be downloaded and added to the simulation. For

galactic magnetic fields, one can choose from toroidal halo field, logarithmic spiral field, or models from [55] and [56]. The user can combine different magnetic fields and set the volume in which one or another field model should be used. So-called magnetic field decorators, which are additional features of the magnetic fields and are used to change the field in the process of propagation, are implemented as well.

Concerning the magnetic field impact, it is possible to decide whether to include the deflection of the particles in the propagation or to neglect it and only consider the magnetic field as a cause of energy loss due to synchrotron radiation.

As 4D galactic propagation is a process that requires significant amount of computation time, the procedure of galactic lensing (using tabulated results from backtracking CR candidates instead of Monte Carlo propagation) is introduced instead of the direct Monte Carlo simulation of such a propagation.

Different interaction modules are available by default. For each interaction, the user should choose the photon background for the CR partice to interact with and decide whether to propagate each type of secondary particles or neglect them. It is possible to choose between internal libraries of CRPropa or rely on external ones for interaction cross-sections. For calculating electromagnetic cascade propagation, user have an opportunity to either adopt Monte Carlo simulations of CRPropa or switch to another Monte Carlo code EleCa [71] or to a transport code DINT [72]. In the DINT code the numerical evaluation of the transport equations is used for photon and electron propagation, and the main difference between CRPropa and EleCa is in the interaction length calculation: in CRPropa it is tabulated independently for each photon background in CRPropa, and in EleCA an overall interaction length resulting from the contribution from each background is used [59].

Propagation of each candidate continues until the user-provided limit is reached. The limit can be put on the properties of propagated particles (e.g. energy, type, position) or on redshift in order to choose the time window for the detection. It is possible to use several limits on different properties at the same time. For 4D simulation, there is an opportunity to introduce space boundary conditions for candidates to save the computation time.

In CRPropa 3 there is a feasibility for the user to define the parameters of the observer. It is possible to detect a particle at the very moment of its creation or at the point when it reaches the observer. The decision of whether to detect or neglect a particle can be made depending on its properties. For 4D simulation, shape and size of the observer can be specified. The user can specify the type of output data (events or trajectories, 1D or 3D) and choose the parameters of the candidate to be recorded from a broad list.

Sources of the cosmic ray candidates can be varied as well. The user can specify the position of the source or the spatial distribution of multiple sources, put limits and spectral index for the initial energy spectrum, determine the type of the initial particles or their composition, make the emission isotropic, specify the source evolution with redshift, etc. If needed, a list of sources can be prepared, or an individual candidate can be described.

CRPropa 3 has special tools to analyze run-time distribution. It has an internal list of constants and units, and, by default, it is working with comoving distances.

3.3 Modification used

The general task of propagating the particles through the galactic magnetic field requires huge amount of computational time, for most of the particles are deflected very significantly. With the detector being a small sphere at the place where Earth resides in the galaxy, in 3D propagation, the particles won't reach the detector at all. For UHECR, however, this task of the galactic propagation is much easier, as particles of ultra high energies are barely deflected and are propagated through the galaxy in a quasi-rectilinear regime. For this reason, and also due to the assumption of the uniform distribution of the sources in space, 1D propagation regime is chosen. Granted, in this thesis, only nuclei of energies above 1 EeV are propagated (see Sec. 4.1), so the impact of the galactic magnetic field is neglected due to extragalactic origin of all the particles.

Since the sources of the UHECR are more or less uniformly distributed at large distances, a random deflection of the particles would have no impact on the isotropic flux, which we are interested in. Due to this symmetry of the problem 1D simulation could be used, with all the deflection due to the extragalactic magnetic field neglected. In this case, there is no reason to use complicated models of the extragalactic magnetic field. The magnetic field is implemented as a vector perpendicular to the propagation axis. The Redshift module is added to calculate the current redshift of the candidate at each step of the propagation.

```
B = UniformMagneticField( Vector3d( 0, Bvalue * nG, 0) )
sim.add( SimplePropagation() )
sim.add( FutureRedshift() )
```

From the variety of photo-hadronic interaction modules, photo-pion production, photo-disintegration (for all initial particles but protons), and nuclear decay are taken into consideration. All the secondary particles are included in the propagation expect for neutrinos. The electromagnetic cascade (pair production, double pair production, triple pair production, inverse Compton scattering), and the synchrotron radiation are considered for electrons and photons. For photon background, CMB, URB [60], and IRB [61] models are used.

```
photons=True
electrons=True
neutrinos=False
nuclei=True

sim.add( PhotoPionProduction( CMB, photons, neutrinos, electrons, nuclei ) )
sim.add( PhotoPionProduction( IRB_Gilmore12, photons, neutrinos, electrons,
    nuclei ) )
sim.add( PhotoDisintegration( CMB, photons ) )
sim.add( PhotoDisintegration( IRB_Gilmore12, photons ) )
sim.add( NuclearDecay( electrons, photons, neutrinos ) )
for background in ( CMB, IRB_Gilmore12, URB_Protheroe96 ):
    sim.add( EMPairProduction(background, electrons) )
    sim.add( EMDoublePairProduction( background, electrons ) )
    sim.add( EMTripletPairProduction( background, electrons ) )
    sim.add( EMInverseComptonScattering( background, photons ) )
sim.add( SynchrotronRadiation( B, False ) )
```

In this thesis, the photon flux above 0.1 EeV is analyzed. Hence, a threshold energy of 0.1 EeV is chosen as the breaking condition for the propagation. No other limits are set up.

```
sim.add( MinimumEnergy( 0.1 * EeV ) )
```

Sources of UHECR are uniformly distributed in the selected comoving distance range. As the aim is to represent realistic 3D case with 1D simulation, geometrical reweighting for uniform distribution on a sphere needs to be done, so every candidate at the end is reweighed with the square of its distance from the observer and normalized. As 1D simulation is unisotropic, and only the number of particles inversely proportional to squared distance would be emitted towards the observer in 3D case, another reweighing is required. These two factors are to cancel each other, so no special geometrical reweighting is required.

```
source.add( SourceUniform1D(Dmin * Mpc, Dmax * Mpc) )
```

Energy spectrum of CR at their sources is set up as power law spectrum with a spectral index of -1. This spectral index has no physics motivation but has rather been chosen to provide better statistics for simulation results at higher energies. Therefore, additional reweighting on the spectral index is done after the simulation to achieve spectral indices of interest. Initial particle type is to be changed from one research task to another, so is the upper limit on the energy spectrum.

```
source.add( SourceParticleType( nucleusId( A,Z ) ) )
source.add( SourcePowerLawSpectrum(Emin * EeV, Emax * EeV, -1) )
```

It is possible to include source evolution with redshift in the propagation, but it could also be done with translating the trajectory length to redshift and doing additional reweighting in 1D case.

In Chapter 5 this part of the code is changed for compositional cosmic ray propagation. In order to add a type of nuclei in the chemical composition, the mass of the nucleus A, its charge Z, and the fraction of this type of nuclei in the total composition at the minimum threshold energy should be specified.

```
composition = SourceComposition( Emin * EeV, Emax * EeV, -1 )
composition.add( A, Z, fraction )
...
composition.add( A, Z, fraction )
source.add( composition )
```

4 Pure proton cosmic rays propagation

"To begin the study of the propagation of hadronic cosmic rays, the sources are assumed to produce only a single type of primary particle. In the simplest case, primary protons are assumed which are the lightest hadrons. Protons do not participate in photo-disintegration, they do not decay, so the number of interactions involved in the propagation is reduced comparing to more heavy nuclei. In the current chapter, step by step we are to come from simple scenarios (one UHECR source, one specific initial energy value) to more realistic ones and predict the UHE photon fluxes from these UHECR sources. This is done to study more precisely the impact of different CR source parameters (e.g. steepness of the initial source energy spectrum) and space parameters (e.g. magnetic field value) on the UHE photon flux on Earth.

From this chapter on, the particles emitted from the sources are called "initial cosmic rays" or "initial particles", the ones produced during the propagation of the initial cosmic rays through space are called "secondary particles", and the flux of the cosmic rays on the top of the Earth's atmosphere is referred as "cosmic ray flux on Earth."

4.1 Discrete distances and discrete energies

In order to have a basic understanding of the impact that UHECR sources at different distances have on the photon flux on Earth, we start the study with the most simple case: one source at specific distance from the observer emits initial CR particles of specific energy. We then have a look at the secondary UHE photon distribution on energy, change the distance and/or the initial energy value and perform the simulation again. The limit on the minimum energy for particles in the propagation is 0.1 EeV, all particles with smaller energy values are excluded from the propagation as soon as they reach this energy value. This is approximately the energy value at which Pierre Auger Observatory can start to detect the CR particles.

Five different initial CR energy values are chosen for this study for better understanding of the impact on the number of photons: 1 EeV, 10 EeV, 50 EeV, 100 EeV, and 400 EeV. 1 EeV is a limit of previous predictions (see Fig. 2.5.1) and also a point where the transition from extragalactic to galactic UHECR is expected, so it is of great interest: if no UHE photons are coming from cosmic rays of this energy, we could assume that all the CRs that are contributing to the UHE photon flux are of extragalactic origin and all the UHE photons are produced before galactic magnetic field influences the CR propagation. 50 EeV is approximately the area of the GZK threshold. 400 EeV is an upper energy limit far above the GZK limit.

Five different distances are chosen as well: 4 Mpc, 10 Mpc, 40 Mpc, 100 Mpc, 400 Mpc. 4 Mpc is the distance to the nearest potential UHECR source, Centaurus A [73]. In general, after $\sim$ 40 Mpc a decrease in the number of photons with increasing the distance is expected. In this research a maximum distance of 400 Mpc is chosen, and other values are roughly equidistant in logarithmic scale.

Results of the simulations are presented in Fig. 4.1.1 and in Table 1. The plots give a general overview on the growth of the photon number with increasing energy value and the non-linear dependency of the number of photons at the observer on the distance from the source. In Table 1

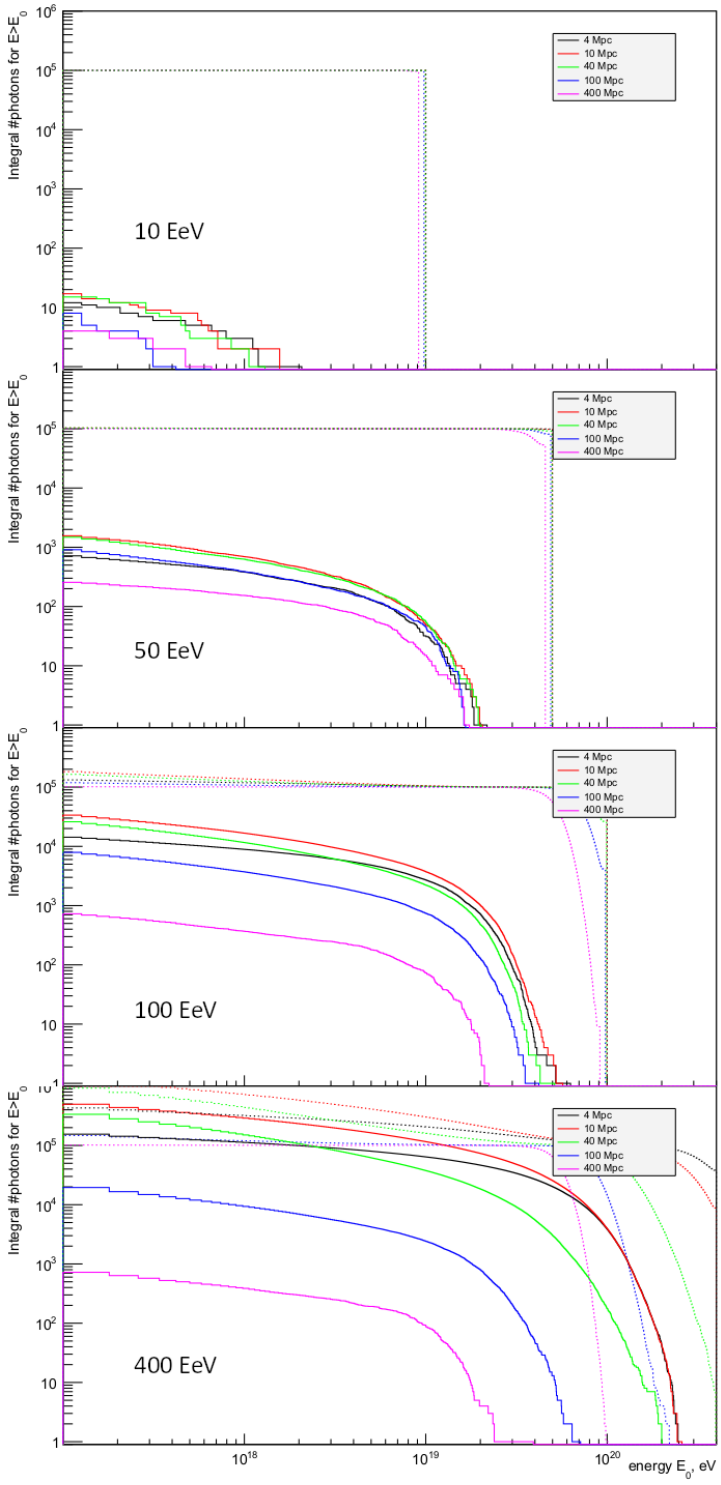

Figure 4.1.1: Integral number of photons reached the detector as the function of the threshold energy E_0. Each plot represents one initial energy value noticed in the plot. Solid lines are the number of UHE photons, and dashed lines are the number of total CR particles for the corresponding energy threshold. The color of the line marks the distance between the source and the observer.

total number of photons is given for each combination of distance and energy value. 10^5 initial particles are emitted in simulations for 10, 50, 100 and 400 EeV. As the case of 1 EeV is of special interest and has an impact on the whole simulation process (the decision on neglecting or including the galactic magnetic field in further propagation is to be made on the basis of this result), 10^7 initial protons are emitted in those propagation. In the Table, however, the number of the UHE photons at the observer is normalized to 10^5 initial particles for more easy comparison with other results. There is no plot for 1 EeV case, as the number of photons is extremely small.

Total amount of UHE photons at the observer point					
energy, EeV	4 Mpc	10 Mpc	40 Mpc	100 Mpc	400 Mpc
1	0.08	0.05	0.05	0.02	0
10	12	17	15	8	4
50	716	1563	1477	910	256
100	14271	33670	25998	7917	727
400	155061	496226	335461	19506	723

Table 1: The number of photons reached the detector from different discrete sources. The number of photons at the detector is normalized to the 10^5 initial protons.

The dependencies observed are easily understandable. The general increase in number of the UHE photons with energy has two main explanations. Firstly, the higher the initial energy, the more interactions proton participates during the propagation (and more secondary particles it produces), see Fig. 2.3.6 for the energy loss length of the nuclei dependence on the threshold energy. Secondly, the higher the energy of the initial, the higher the energy of the secondary photon, so more of them end up in the energy range of interest. When it comes to distances, the maximum is reached at distances in a range from 10 to 40 Mpc. 4 Mpc is too small distance for majority of the UHE protons to participate in several (for 10 EeV even one) interactions. With distances of 100 Mpc or even 400 Mpc protons lose too much energy during all the interactions they take part in, so the photons produced there have too small energies; and the photons produced in very first interactions are so far away from the detector that they mostly interact with the photon background before reaching Earth. Both the number of the total CR particles and UHE photons is smaller for 100 Mpc and 400 Mpc then for 40 Mpc (for the considered energies).

The main conclusion we are to make from this study is that initial cosmic rays with initial energies lower than 1 EeV contribute negligibly in the number of UHE photons with energies above 0.1 EeV. Thus, these CRs can be safely expelled from the propagation in order to save computation time. As the energy range around 1 EeV is the range in which galactic CR flux is being exceeded by extragalactic one, we can consider all our initial particles of extragalactic origin. Other important features of the UHE photon flux dependency on the distance of the source and the initial energy of the CR particles are the increase of the flux with distance up to 10-40 Mpc and decrease of the flux with further increasing distance, and a general increase of the total number of UHE photons with energy (effect is larger for smaller distances).

4.2 Parameters study

As there is no direct and precise understanding of neither sources of the UHECR propagation, nor space parameters (e.g. magnetic field, photon background), a benchmark scenario is needed for further research. Variation of its parameters is to give an idea of possible systematic uncertainties inherited from a lack of knowledge about these parameters' values.

In all further simulations of this chapter CR sources are uniformly distributed within a distance range from 4 Mpc to 2800 Mpc in coherence with [9]. A suitable choice of the upper limit is re-evaluated later in this section. The assumption is made that sources have similar energy spectrum of emitted primaries with power law dependency and a rigidity cut-off:

$$\frac{\mathrm{d}N}{\mathrm{d}E}(E) \propto E^{-\alpha} / \cosh(E/R_{\text{cut-off}}) \tag{4.1}$$

where α is the spectral index, and $R_{\text{cut-off}}$ is a maximum rigidity value.

The energy spectrum of CR at their sources in this subchapter has following parameters: spectral index $\alpha = 2$, maximum rigidity $R_{\text{cut-off}} = 10^{20}$ eV, minimum energy of 1 EeV and maximum energy of 400 EeV. A suitable choice of the upper limit is re-evaluated in Sec. 4.3.

Propagation is simulated in the absence of magnetic fields and with no source evolution with redshift in coherence with [9]. For photon background CMB, URB [60] and IRB [61] models are used. Total CR flux received at the observer is normalized to the results of the Pierre Auger Observatory from [74] at energy value of 10^{19} eV, see Fig. 4.2.1.

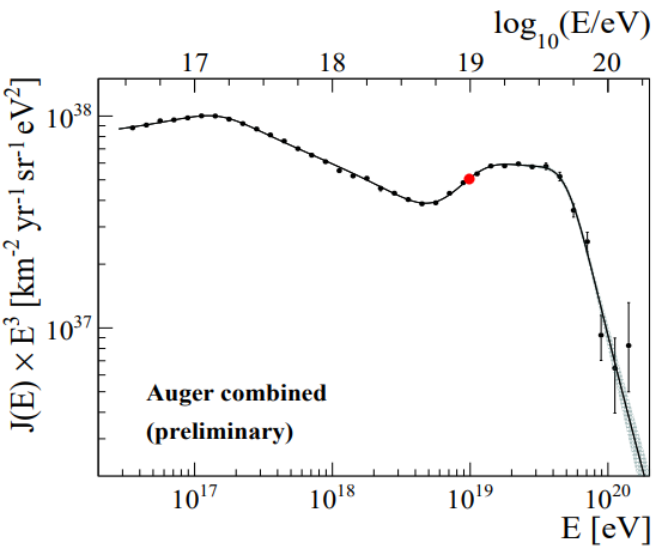

Figure 4.2.1: Preliminary energy spectrum of the CR observed at the Pierre Auger Observatory [74]. The red point is the normalization value used in the thesis.

As the aim of this study is to get a better understanding of the impact of each parameter of the propagation scenario on the UHE photon flux, we are going to vary them one by one and look at the fluxes and at the fraction of UHE photons in the total CR flux received at the observer. Parameter values are mostly taken from [9] for easier comparison of the results.

One notification should be done for all future results. On the plots fluxes are shown in a threshold energy range from 0.1 EeV, as this is the limit we are aiming to give predictions for, yet the initial CR spectrum, as was discussed above, have a minimum of 1 EeV. If we were to present the results with no corrections, the artificial kink at E_0 =1 EeV in CR fluxes would had been observed, and the photon fractions would had had artificial kinks at that energy. As there is no physical meaning behind those features, correctional reweighting in in the energy bins between 0.1 and 1 EeV is done for total cosmic ray fluxes.

The first parameter to discuss is the **spectral index**. Spectral index α from Eq. 4.1 is changed in a range from $\alpha = 1$ to $\alpha = 3$. The impact of these changes is demonstrated in Fig. 4.2.2. In the integral photon flux, the general decrease of the flux with the increase of the spectral index is noticeable. The difference between UHE photon fluxes is almost an order of magnitude, independently of the threshold energy E_0. Integral total CR flux increases with the spectral index at lower energies and decreases with increasing spectral index at higher ones (due to normalization at 10^{19} eV). Photon fraction is also decreasing with growth of the spectral index, yet the difference is significantly larger for lower energies than for higher ones.

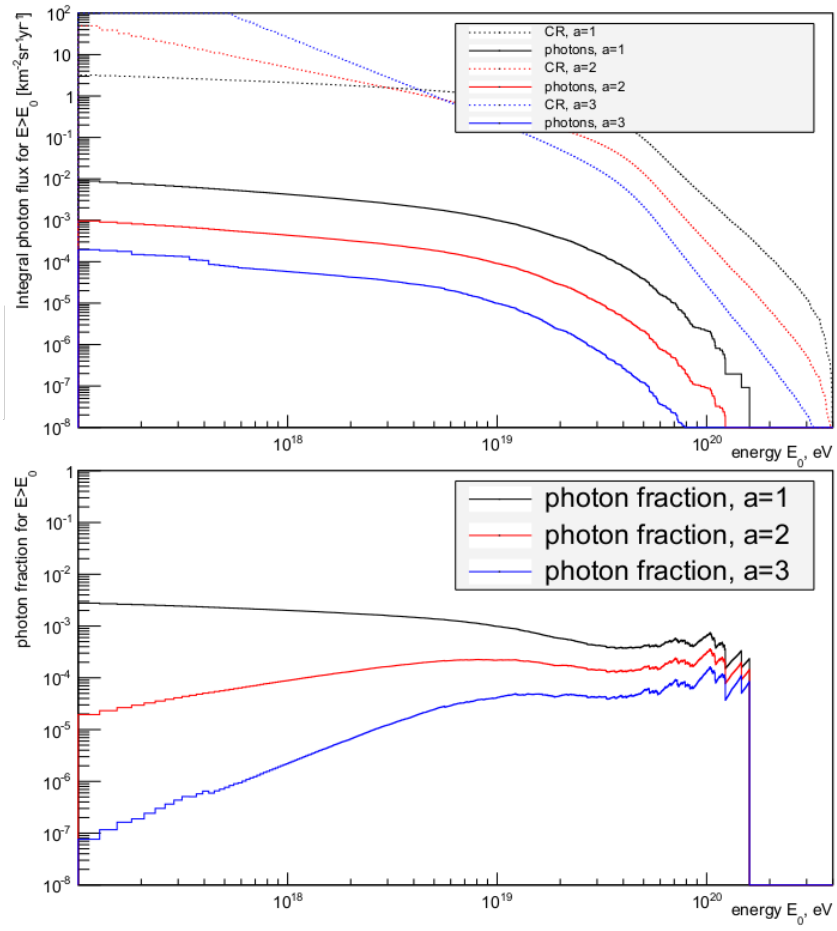

Figure 4.2.2: Impact of the spectral index of the initial energy spectrum of the sources on the UHE photon flux. *Top:* Integral photon fluxes (with total CR fluxes in dashed lines) in dependency of the threshold energy E_0. *Bottom:* Integral UHE photon fraction in dependency of the threshold energy E_0.

This happens, as with increasing the spectral index we bring more protons with lower energies

and less protons with higher energies into simulations. The total CR flux on Earth is then changing accordingly, and as is concluded from discrete sources study in Sec. 4.1, protons with less initial energies create less UHE photons while being propagated, so the fraction of UHE photons increases significantly with initial proton energy. The impact of the spectral index on the fraction of photons in the total CR flux on Earth is not as significant for higher energies of the particles, as it is for lower ones due to the total CR flux behaviour.

Initial spectrum of the sources also depends on the **maximum rigidity**. In this study $R_{\text{cut-off}}$ is changed from 10^{19} eV to 10^{20} eV and then to 10^{21} eV. The results are shown in Fig. 4.2.3. Maximum rigidity value determines, at which energies the initial particles spectrum starts being

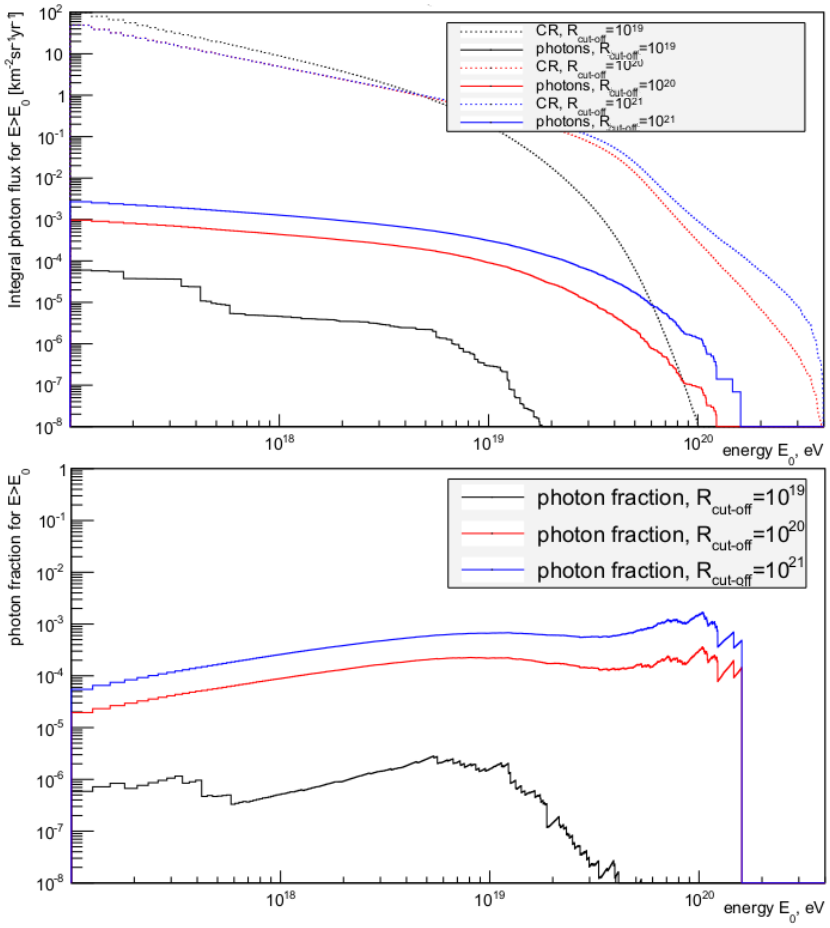

Figure 4.2.3: Impact of the maximum rigidity of the initial CR energy spectrum at their sources on the UHE photon flux. *Top:* Integral photon fluxes (with total CR fluxes in dashed lines) in dependency of the threshold energy E_0. *Bottom:* Integral UHE photon fraction in dependency of the threshold energy E_0.

suppressed, so with increasing of the maximum rigidity more and more UHE photons coming from initial protons with higher energies are included into the flux, and with normalization the weight of initial cosmic rays with lower energies and their secondary particles is decreasing accordingly. As was described above, this leads to general increase of the UHE photon flux. Flux and photon fraction for $R_{\text{cut-off}} = 10^{19}$ eV is notably smaller than ones for other values, as suppression starts already at 10 EeV in this case. This energy value is much lower than the threshold energy for the GZK interaction. Therefore, the majority of the protons that can par-

ticipate in this main photo-hadronic process, are strongly suppressed, and less GZK interactions means less GZK photons.

Another parameter concerning sources is the **maximum source distance**. Study of the impact of distant sources on the UHE photon flux is performed as follows: the propagation of UHECR from sources to Earth with sources being uniformly distributed in the range from 4 Mpc to 3600 Mpc is done, and then the contribution of distant sources is explored by changing the upper limit of the distance range. Limits of 10 Mpc, 30 Mpc, 100 Mpc, 300 Mpc, 1000 Mpc, 2000 Mpc, and 3600 Mpc are studied. In Fig. 4.2.4 the results are shown.

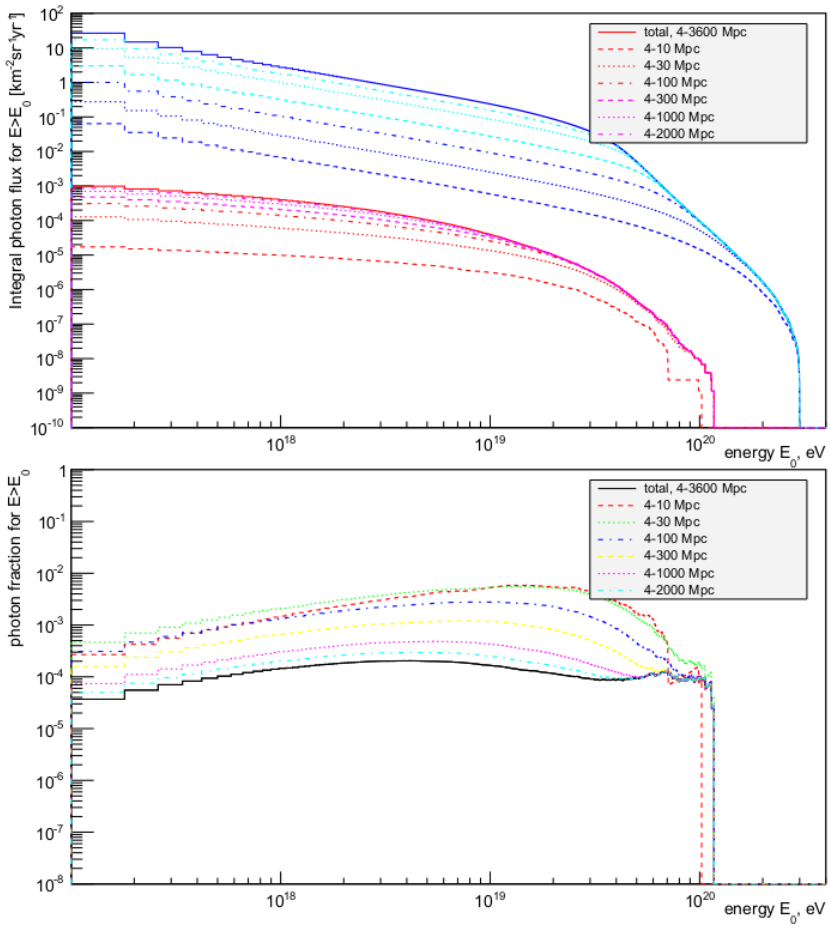

Figure 4.2.4: Impact of the upper limit of included source distances of the initial energy spectrum of the sources on the UHE photon flux. *Top:* Integral photon fluxes (with total CR fluxes in dashed lines) in dependency of the threshold energy E_0. *Bottom:* Integral UHE photon fraction in dependency of the threshold energy E_0.

From the fluxes, it is apparent that while the range of 4-10 Mpc does only contribute $\approx$ 2% of the overall flux from the whole 4-3600 Mpc range, the dependency of the UHE photon flux on the maximum source distance is highly non-linear, and the UHE photon flux coming from the sources in the range of 4-2000 Mpc is almost as big as the whole flux. To understand the dependency of the contribution to the total flux on maximum source distance better, the ratio of the number of photons coming from each of discussed areas to the one of the whole 4-3600

Mpc range is shown in Fig. 4.2.5. Point of maximum source distance 2800 Mpc, the benchmark scenario value, is also included here.

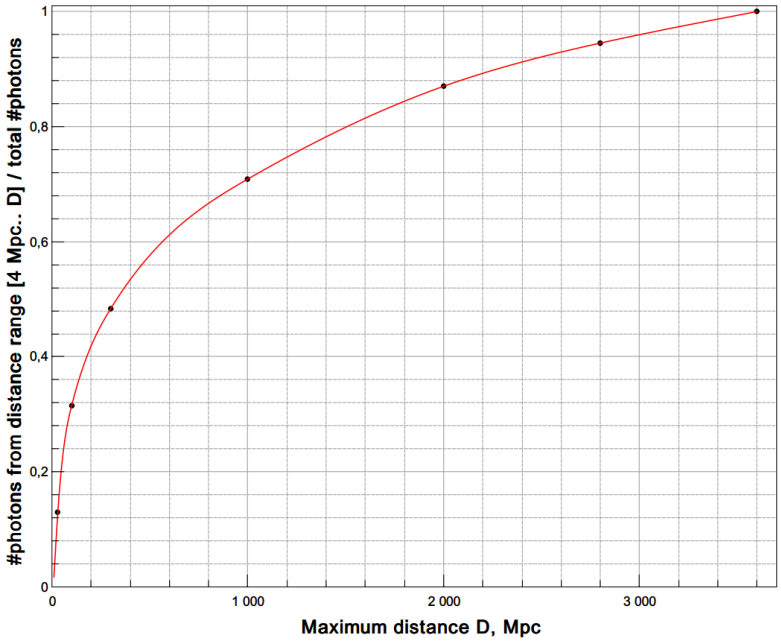

Figure 4.2.5: Ratio of area's contribution to the total UHE photon flux (the flux from a distance range of 4-3600 Mpc) as a function of the maximum source distance. Red line is a cubic spline.

With this dependency, it is easier to understand the possible uncertainties one may have from excluding the far-distant sources from the propagation. These uncertainties are significantly smaller than the uncertainties that are introduced by the choice of the spectral index or the rigidity cut-off. With an upper limit on source distances of 2800 Mpc, we are losing less than 6% of the UHE photons compared to the flux coming from the 4-3600 Mpc range, so this is a proper point of balance between saving computation time and lowering down the uncertainties of the simulation.

Also, fluxes in Fig. 4.2.4 indicate that far-distant sources do not contribute at all to the total flux at higher threshold energy. Photons with energies higher than 30 EeV are only coming from sources closer than 100 Mpc from the observer. This is, as was discussed in Sec. 4.1, due to finite photon interaction length and CR particles losing energy while being propagated.

Cosmological effect of **density and luminosity of the sources evolving with redshift** has also been studied. As mentioned in Sec. 2.2, this evolution is different for different sources of UHECR. Three scenarios are compared here - the uniform distribution with no evolution, the one with evolution following the star formation rate (SFR) and the steeper one for quasar-like systems (QS). The results are presented in Fig. 4.2.6. As the evolution follows the formula $(1 + z)^m$ with m = 0 for uniform distribution of the sources, m = 3.4 for SFR and m = 5.5 for quasars, and redshift z is growing with distance [75], the evolution in general give more weight to far-distant sources. From previous parameter study, we know that far-distant sources contribute less to the overall photon flux on Earth, so the decrease in all the UHE photon flux is expected and noticeable in the plot. UHE photon flux from sources with SFR type of evolution is nearly two times higher than the one from sources with QS type of evolution and nearly two

times lower than the one from sources with no evolution.

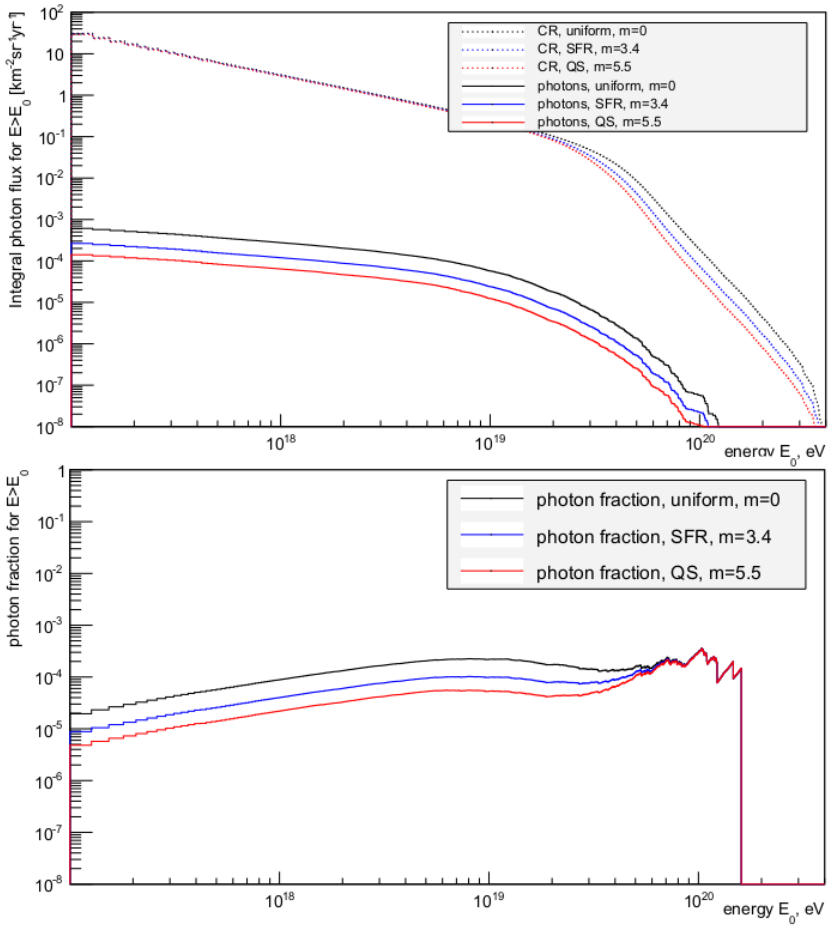

Figure 4.2.6: Impact of the source evolution with redshift on the UHE photon flux. *Top:* Integral photon fluxes (with total CR fluxes in dashed lines) in dependency of the threshold energy E_0. *Bottom:* Integral UHE photon fraction in dependency of the threshold energy E_0.

Besides the parameters of the sources, ones of the space should be discussed as well. **Magnetic field** in this propagation is only included in synchrotron radiation process, all the deflections are neglected. As was explained in Sec. 3.3, extragalactic magnetic field is implemented as a uniform vector perpendicular to the propagation direction, so only the absolute values are discussed here. Extragalactic magnetic field value of 0.34 nG is representing the model from [57], the value of 15 nG is for the model from [58]. Propagation in the absence of magnetic fields and the case of 1 nG field are added for more clear understanding of the dependency. Magnetic fields are mainly affecting electrons and positrons, so these particles lose their energy and don't produce photons of ultra-high energy in inverse Compton scattering or triplet pair production. The general decrease of the UHE photon flux with increasing the magnetic field is noticeable in Fig. 4.2.7.

The stronger the magnetic field, the larger are the losses on synchrotron radiation, so the impact becomes more significant. The effect disappears with increasing of the threshold energy, as photons with the highest energies are generally the ones which come directly from photo-hadronic interactions and don't lose energy on further interactions with the background, so their energies

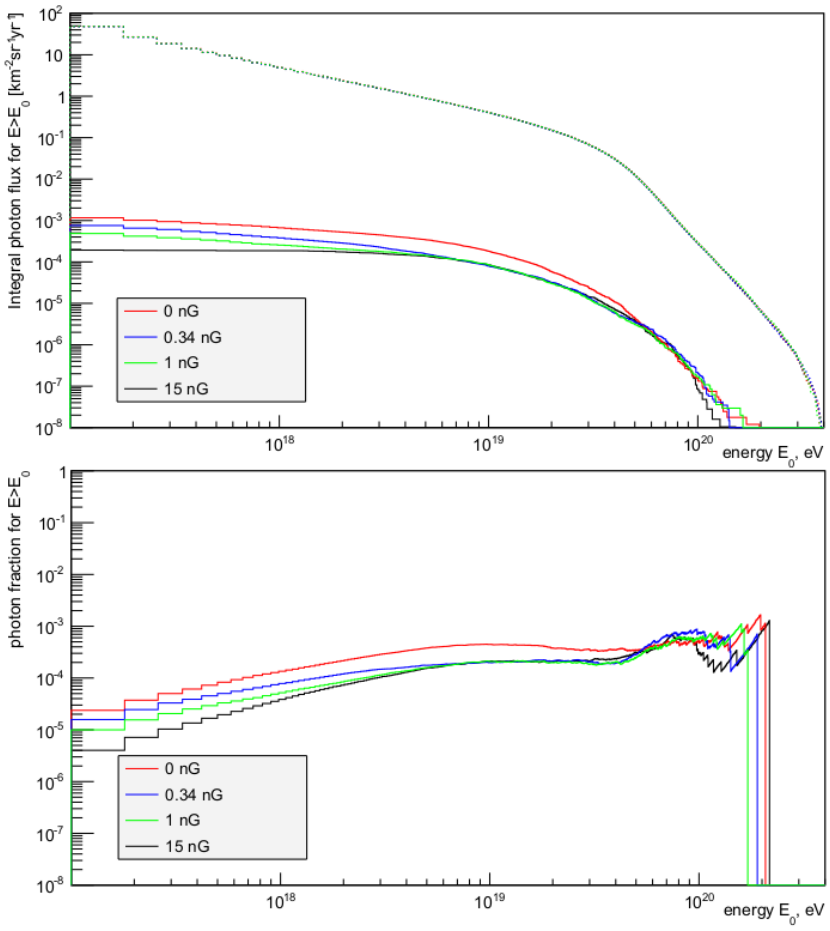

Figure 4.2.7: Impact of the magnetic field value on the UHE photon flux. *Top:* Integral photon fluxes (with total CR fluxes in dashed lines) in dependency of the threshold energy E_0. *Bottom:* Integral UHE photon fraction in dependency of the threshold energy E_0.

are not dependent on electrons losing energy to synchrotron radiation. In other words, the effect of the magnetic field is larger for those UHE photons that are produced deeper in the EM cascade.

Remaining parameter of the space is the **universal radio background**. The result of the propagation in absence of URB is compared to the one with URB of Protheroe's model [60]. It is noticeable from Fig. 4.2.8 that URB has no significant impact on total CR flux, yet photon flux is lower when URB is taken into account. As was mentioned in Sec. 2.3.2, URB has the smallest average energy per photon, and the threshold energy for the interactions of UHECR with photons of this background is the highest of all (e.g. for GZK-process it is larger than 100 EeV). Photo-hadronic interactions in current energy range are then almost only happening with the cosmic microwave background and infrared background light, and only for the most energetic protons the absence of URB is noticeable. This means that without URB less amount of UHE photons with highest energies is produced, but for CR particles with initial energy less than 100 EeV the existence of the URB is not important. This lack of the UHE photons is distinguishable in Fig. 4.2.8, and the effect is increasing with energy, as expected.

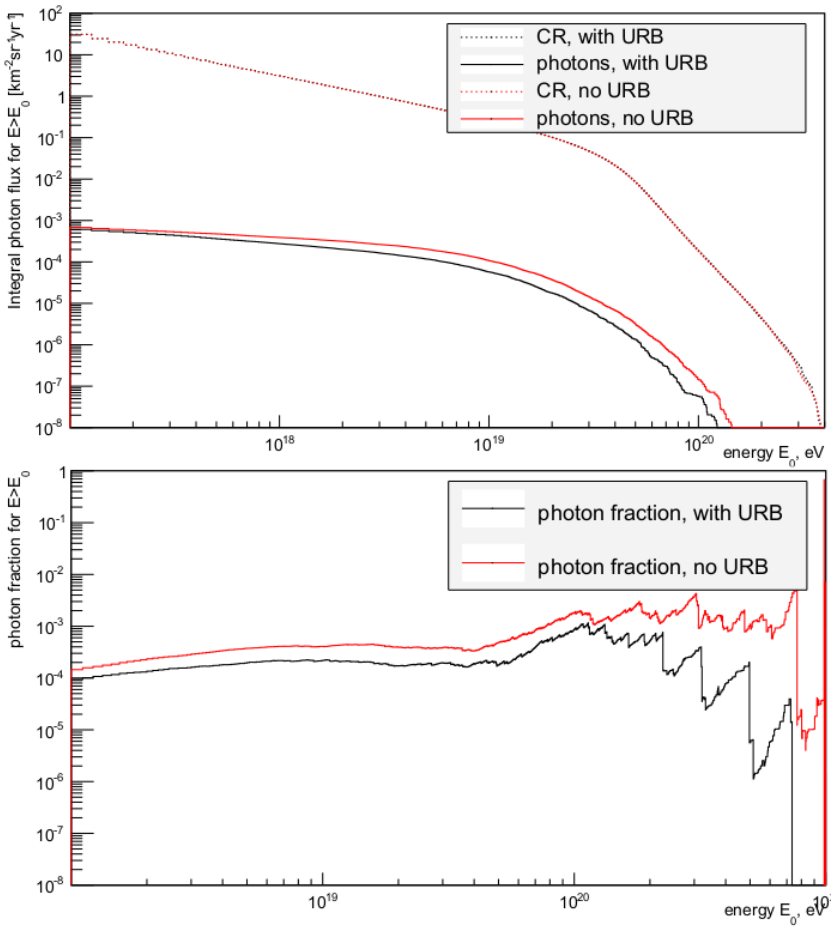

Figure 4.2.8: Impact of the universal radio background on the UHE photon flux. *Top:* Integral photon fluxes (with total CR fluxes in dashed lines) in dependency of the threshold energy E_0. *Bottom:* Integral UHE photon fraction in dependency of the threshold energy E_0.

One last propagation parameter to check is the impact of the **electron pair production** (EPP) on the simulation. This photo-hadronic interaction, as described in Sec. 2.3.2, may have some impact on the UHE photon flux. The question here is whether it is necessary to include this interaction in the simulation, or it can be omitted to save computing resources. Including this particular interaction significantly increases the computational time, and is not supposed to be dominant in the energy area of interest [65]. As electrons play significant role here, magnetic field of 0.34 nG is included into benchmark scenario for this one study.

The impact of the electron pair production is shown in Fig. 4.2.9. According to the plot, electron pair production has only a minor impact on the total CR flux. In CRPropa 3 electron pair production is implemented as energy loss process for hadronic nuclei, and the electron-positron pairs are produced out of that lost energy [76]. And as it is mostly impacting nuclei of 10-50 EeV, for total CR flux it would mean fewer particles in this range, and more in the range below 10 EeV and above 50 EeV (again, due to the normalization at 10^{19} eV). The influence of the EPP process on the UHE photon flux is, however, small. The UHE photon flux with EPP involved is generally slightly higher, because EPP is a weak source of secondary photons: electrons produced in EPP can then possibly interact with background photons and produce

UHE photons. The difference in fraction of the UHE photons in total CR flux above 20 EeV is caused by the changing behaviour of the total CR flux in this energy range.

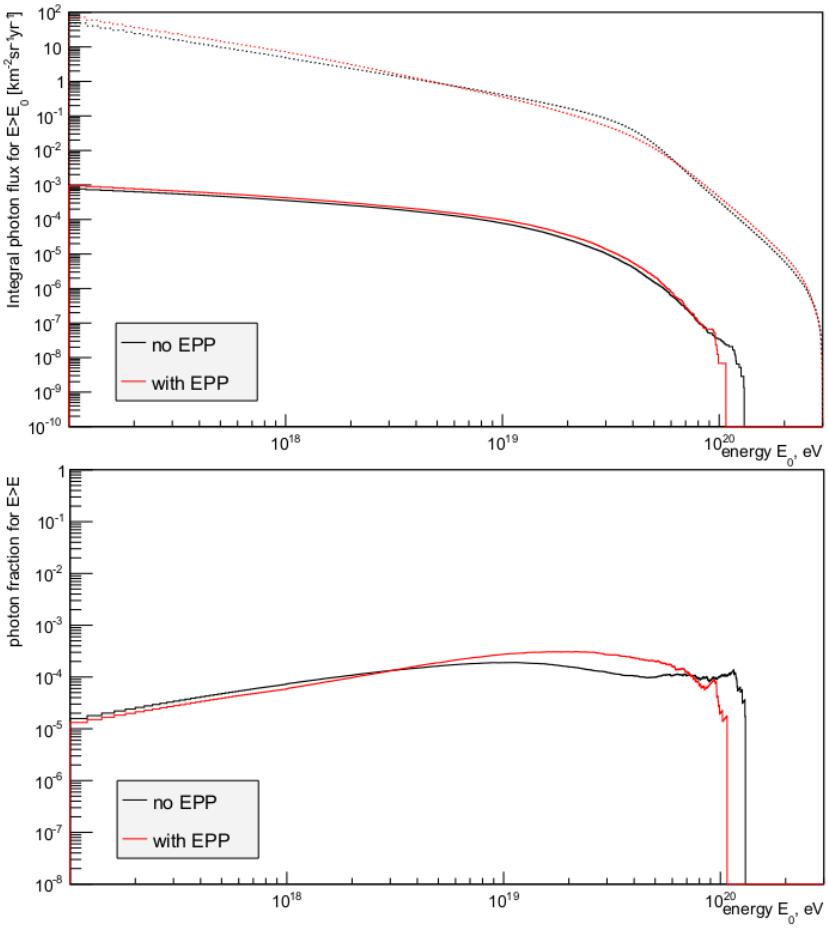

Figure 4.2.9: Impact of the electron pair production process on the UHE photon flux. *Top:* Integral photon fluxes (with total CR fluxes in dashed lines) in dependency of the threshold energy E_0. *Bottom:* Integral UHE photon fraction in dependency of the threshold energy E_0.

In further propagation, the EPP process is excluded from the list of the interaction, yet it should be considered that, for pure protons, the flux may be $\sim$ 15% higher for spectral index $\alpha = 2$, if EPP is included. The impact becomes more significant with increasing the spectral index. For spectral index $\alpha = 1.7$ the photon flux is $\sim$ 9% higher with the EPP process included. The highest spectral index used in current thesis is $\alpha = 2.1$, and for the scenario in which this index appears (see Sec. 4.3), adding the EPP process to the propagation would lead in UHE photon flux higher by $\sim$ 17%.

All the dependencies observed are in agreement with the expectations and are not significantly different from previous results shown in [9].

4.3 Realistic scenarios

Previously parameters of the propagation were mostly chosen to show the uncertainty ranges, but their astrophysical credibility was not questioned so far. To give more reliable predictions of UHE photon flux, two more realistic scenarios of propagation, 'low' and 'high', are to be created. Parameters values for these scenarios are taken from [9].

- scenario 1, *higher flux*: spectral index $\alpha = 1.7$, maximum rigidity $R_{\text{cut-off}} = 10^{19.5}$ eV, evolution following star formation rate (m=3.4), magnetic field of 0.34 nG (Dolag et al [57])
- scenario 2, *lower flux*: spectral index $\alpha = 2.1$, maximum rigidity $R_{\text{cut-off}} = 10^{19.6}$ eV, evolution as indicated for quasars (m=5.5), magnetic field of 15 nG (Miniati et al [58])

Sources from distances of minimum 4 Mpc and maximum 2800 Mpc are taken into account. The last parameter to configure is the upper limit for source energy spectrum. It is important, on one side, to choose this limit large enough to have a trustworthy UHE photon flux on Earth, and on the other side, to not overestimate this value, as it has the most significant impact on the computation time. This parameter is checked for the 'high' propagation scenario. Propagation results for four different upper limits are shown in Fig. 4.3.1. Impact is only observed at the highest threshold energy values, where the UHE photon fluxes are of very low values. The choice of this upper limit depends on the uncertainties allowed in the resulting flux. For further propagation the limit of 300 EeV[1] is chosen.

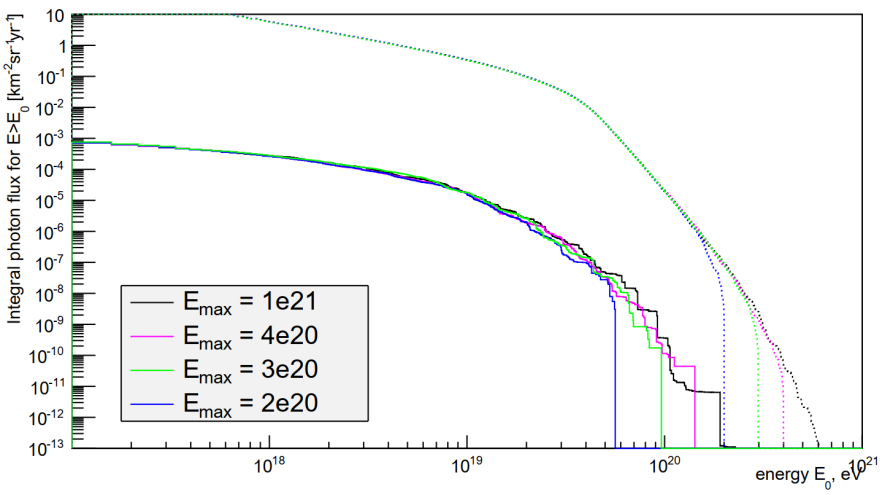

Figure 4.3.1: Impact of the upper limit of the source energy spectrum on the UHE photon flux. Integral photon and total CR fluxes in dependency of the threshold energy E_0.

The resulting prediction of the pure proton cosmic rays study is shown in Fig. 4.3.2. The prediction is far (two to five orders of magnitude depending on the energy) below the upper limits derived from experimental data. It is also by two orders of magnitude below the previous model prediction from [8], yet the parameters of the propagation scenarios are different. If comparing

[1]This choice of the energy limit coincides with the energy of the Fly's Eye particle detected by High Resolution Fly's Eye Cosmic Ray Detector, the particle with highest-ever-detected energy [77].

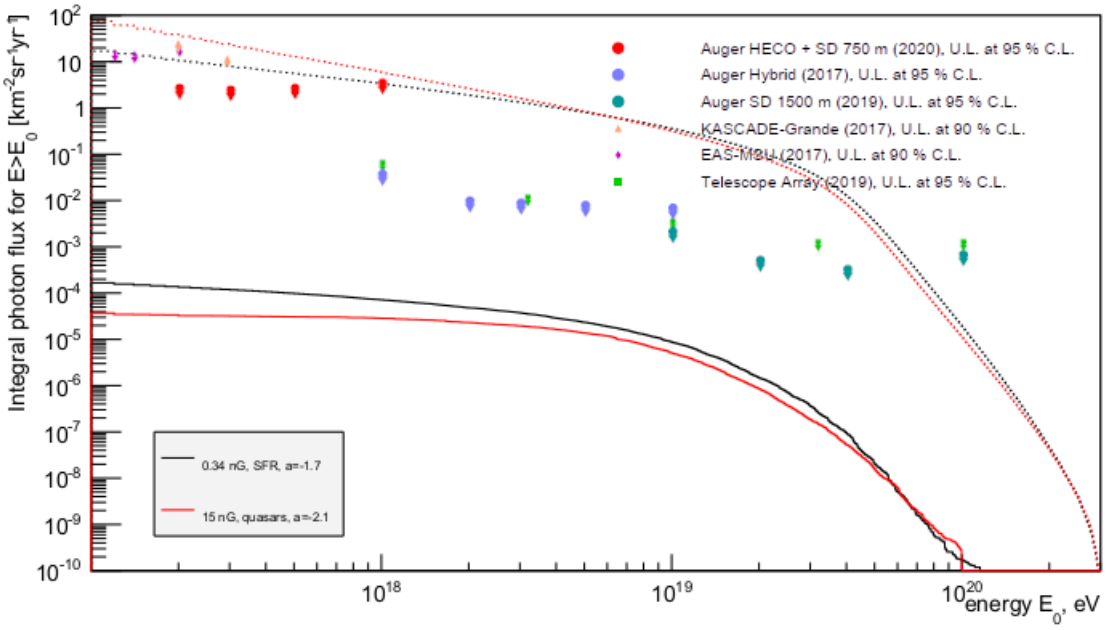

Figure 4.3.2: Prediction of the UHE photon flux from pure proton cosmic ray propagation. Integral photon and total CR fluxes in dependency of the threshold energy E_0. Limits from the Pierre Auger Observatory [78], [67], [79], KASCADE-Grande [4], EAS-MSU [6], TA [5].

to the results from [9], the difference is less significant here, yet the results are still slightly below previous ones. Concerning the propagation parameters, the only difference between current scenarios and the ones used in [9] is in the IRB model, switching from Kneiske'04 [80] model to Gilmore'12 [61] one, yet it has negligibly small impact on the results. Normalization of the results was made to the data published in 2013 in [81], and in the current thesis it is to the data from 2019 from [74], yet the value of the energy spectrum at 10^{19} eV is almost the same. The main reason for the differences may be the new configuration of CRPropa framework (CRPropa 2 used in [9] and CRPropa 3 used in the current thesis). The whole structure of the framework was changed in this upgrade, and also the implementation of the photo-pion production, main interaction of the research, was improved (interaction rates recalculated, cross-sections for wider energy range added), and the transition to internal usage of comoving distances was made [70]. These changes in CRPropa 3 may account for the differences between the results in [9] and current work.

5 Heavy nuclei cosmic rays propagation

5.1 Pure heavy nuclei cosmic ray propagation

When turning to the propagation of heavier cosmic ray particles, the photo-hadronic process of photo-disintegration is added. This process has been found to have significant impact on both CR and UHE photon fluxes. To understand this impact better the propagation of UHECR consisting of only one element is made for several different elements. As a benchmark scenario the 'higher' scenario of pure proton propagation is chosen. Both upper limit on source energy and maximum rigidity are now proportional to the charge of the nucleus Z.

$$\frac{\mathrm{d}N}{\mathrm{d}E}(E) \propto \frac{E^{-\alpha}}{\cosh(E/(R_{\text{cut-off}}(^1\mathrm{H})\,Z))} \tag{5.1}$$

$$E_{\max}(\mathcal{N}) = E_{\max}(^1\mathrm{H})\,Z \tag{5.2}$$

The results of the simulation for ${}^{1}_{1}$H, ${}^{4}_{2}$He, ${}^{11}_{5}$B, ${}^{14}_{7}$N, ${}^{28}_{14}$Si, ${}^{40}_{18}$Ar and ${}^{56}_{26}$Fe initial CR nuclei are shown in Fig. 5.1.1.

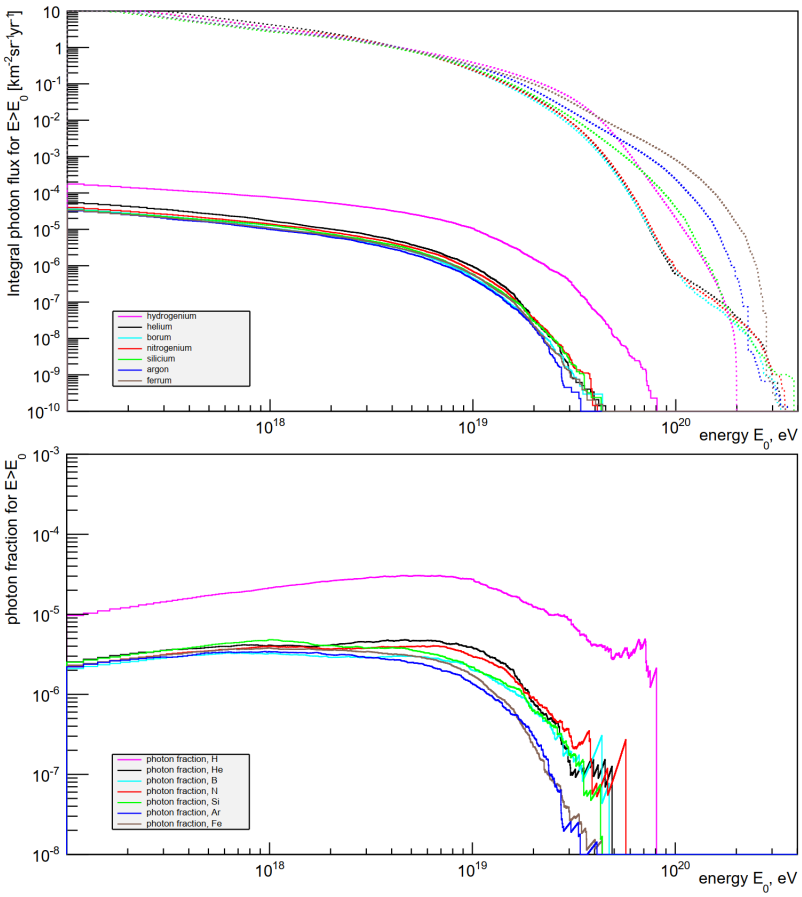

Figure 5.1.1: Impact of the mass of the initial nuclei on the UHE photon flux. *Top:* Integral photon fluxes (with total CR fluxes in dashed lines) in dependency of the threshold energy E_0. *Bottom:* integral UHE photon fraction in dependency of the threshold energy E_0.

Protons do not participate in photo-disintegration, so the fluxes observed from initial cosmic rays consisting of pure ${}^{1}_{1}$H are the same as in Chapter 4. For all the heavier nuclei photo-disintegration is a dominant process, as heavy nuclei decay fast (see Fig. 2.3.4 for the photo-disintegration mean free path) into lighter ones, and at the observer most of the hadronic particles are protons. As shown in Fig. 2.3.4, the heavier the nucleus is, the smaller is the mean free path.

In the total CR flux in Fig. 5.1.1 a kink appears for pure He initial CRs at ~ 100 EeV, then with increasing the charge of the initial nuclei the kink slowly becomes less and less sharp, moves to higher energies and almost disappears for heavy initial CRs. This kink represents the decay of the nuclei via photo-disintegration. At this point one high-energetic nucleus decays into several nuclei with less energy, and the lighter the initial CR nucleus is, the more critical is this step. This is due to the fact that, while He through photo-disintegration decays symmetrically into two particles twice less massive, Fe nucleus, as shown in Fig. 2.3.3, has asymmetrical step by step decay, so the decrease in the main nucleus' energy is less steep. And as for UHE photon flux, as the energy per nucleon is higher in protons than in other elements, more UHE photons are produced in propagation of protons, while the difference between all UHE photon fluxes produced by heavier nuclei is almost insignificant, and there is no strong dependency on the charge or mass of the initial nuclei. Results of the more precise study of the dependency of the UHE photon flux on Earth on the charge of the initial CR nuclei are shown in Fig. 5.1.2. Lines here are linear splines to lead the eye. General decrease is seen, yet from element to element no clear trend is visible.

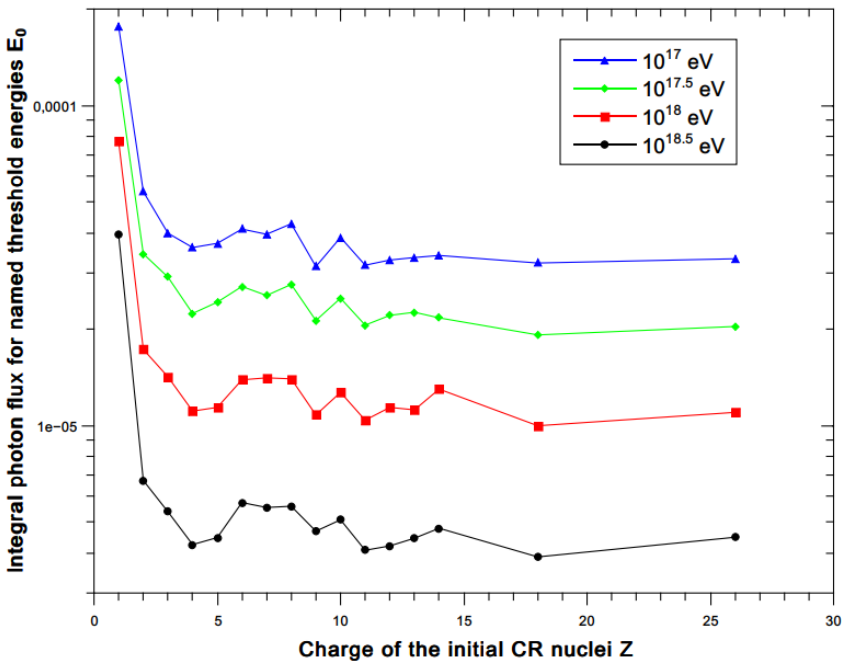

Figure 5.1.2: Integral UHE photon flux value for the threshold energy E_0 named in the legend as a function of the charge of the initial CR nuclei. Lines are linear splines to lead the eye.

As a result of this study, in Fig. 5.1.3 the UHE photon fluxes from initial protons (red) and initial iron nuclei (blue) are shown for both 'higher flux' and 'lower flux' scenarios from Sec. 4.3. These two scenarios represent an estimation of the uncertainties due to the choice of propagation parameters, so the areas between those lines can be considered as the prediction of the UHE

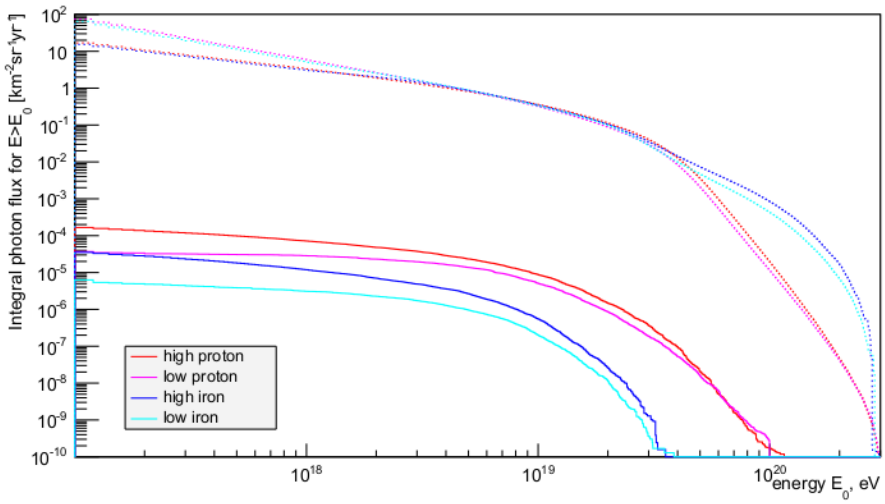

Figure 5.1.3: Integral UHE photon flux from proton (red) and iron (blue) initial cosmic rays in dependency of the threshold energy E_0.

photon flux from those cosmic rays.

5.2 Mixed cosmic ray propagation

5.2.1 Combined fit of the spectrum and composition data

Analysis of the depth $X_{\max}$ of maximum development of the shower in the atmosphere received at the Pierre Auger Observatory shows that the composition of initial cosmic rays changes for different energies [82]. For instance, the CR flux on Earth at energy less that 1 EeV is expected to be produced from initial pure proton CRs, and for the highest energies pure iron initial CRs could describe the observations. However, the CR flux on Earth in energy range approximately from 1 EeV to 100 EeV is believed to be a result of the propagation of mixed cosmic rays from their sources towards Earth, see Fig.6 in [74]. Several general expectations exist on the parameters of these initial cosmic rays (like hard spectrum with spectral index $\alpha \approx 1 - 1.6$ at the sources and low maximum rigidity $R_{\text{cut-off}} < Z \times 5\,\text{EeV}$ [83]). Yet to provide a parameter set of the initial cosmic rays (spectral index, maximum rigidity, fractions of different elements in the initial composition) that would lead to observed CR flux on Earth, a detailed fitting procedure needs to be performed.

One attempt to create such a parameter set is described in [82]. The results of this analysis relevant to the current study are compiled in Table 2. The values derived in this fit may be used as parameters for the propagation scenario. Then the UHE photon flux predictions can be obtained for the mixed initial cosmic rays.

The fit procedure in which these values were derived happened as follows. First of all, the two independent sets of data (energy values of the particles on the top of the Earth's atmosphere and $X_{\max}$ distributions) from the Pierre Auger Observatory were selected. Then the benchmark propagation scenario was created with several assumptions made to save computational time and

Best-fit parameters of the mixed UHECRs						
parameter	Likelihood scanning				Posterior sampling	
	main minimum		2nd minimum			
	best fit	average	best fit	average	best fit	shortest 68% int.
α	0.96	0.93 ± 0.12	2.04	$2.05^{+0.02}_{-0.04}$	1.22	$1.20 \div 1.38$
$\log_{10}(R_{\text{cut-off}}/eV)$	18.68	18.66 ± 0.04	19.88	19.86 ± 0.06	18.72	$18.69 \div 18.77$
$f_{\text{H}}(\%)$	0.0	$12.5^{+19.4}_{-12.5}$	0.0	$3.3^{+5.2}_{-3.3}$	6.4	$0.0 \div 18.9$
$f_{\text{He}}(\%)$	67.3	$58.6^{+12.6}_{-13.5}$	0.0	$3.6^{+6.1}_{-3.6}$	46.7	$18.9 \div 47.8$
$f_{\text{N}}(\%)$	28.1	$24.6^{+8.9}_{-9.1}$	79.8	$72.1^{+9.3}_{-10.6}$	37.5	$30.7 \div 51.7$
$f_{\text{Si}}(\%)$	4.6	$4.2^{+1.3}_{-1.3}$	20.2	$20.9^{+4.0}_{-3.9}$	9.4	$5.4 \div 14.6$
$f_{\text{Fe}}(\%)$	0.0		0.0		0.0	
p-value	0.026		0.0005		$\approx$0.06	

Table 2: Best-fit parameters for the reference scenario [82]. Errors are from the fitting procedures, systematic ones are only included for Posterior sampling, their calculation is described in the paper.

7 independent parameters unsettled. The scan over these parameters was made: the simulations of CR propagation were performed according to the benchmark scenario and with these 7 parameters being changed. After that two different statistical approaches, likelihood scanning (LS) and posterior sampling (PS), were used to derive the optimal fit parameters of the benchmark scenario, so the resulting CR flux on Earth would fit the experimental data best.

Now each of the steps of the fitting procedure are to be described in more details. First of all, the data sets were selected from the observations of the Pierre Auger Observatory with usage of both surface and fluorescence detectors. For the energy spectrum at the ground level only the data from surface detectors was used. No regular reconstruction of the energy spectrum at the ground level was made from the observed counts. Instead, the simulations of the spectrum at the ground level with different propagation scenarios were made, expected event count in each energy range was calculated, and then simulated event counts were directly compared to the observed counts. The $X_{\max}$ distributions were received from the fluorescence telescopes. The Gumbel parameterization was used to derive the mass composition from these distributions. The method is described in details in [84].

Next step was the benchmark scenario of the CR propagation from their sources towards Earth, and here several assumptions needed to be made. Only a representative set of injected elements was taken into account (^{1}H, ^{4}He, ^{14}N, ^{28}Si and ^{56}Fe), which leaded to 4 independent fit parameters of the fractions f_A for 4 elements, and fifth one was derived from the sum of all the fractions equal 1. The fraction values were defined for integral initial spectrum of the CR at their sources at fixed threshold energy of 1 EeV. Sources of the UHECR were assumed to be identical, uniformly spread and isotropically emitting. The spectrum of the cosmic rays at the sources for each of the elements A was described with the function:

$$\frac{dN_A}{dE} \propto f_A E^{-\alpha} f_{\text{cut-off}}(E, Z_A R_{\text{cut-off}}), \tag{5.3}$$

$$f_{\text{cut-off}}(E, Z_A R_{\text{cut-off}}) = \begin{cases} 1 & (E < Z_A R_{\text{cut-off}}) \\ \exp\left(1 - \frac{E}{Z_A R_{\text{cut-off}}}\right) & (E > Z_A R_{\text{cut-off}}) \end{cases} \tag{5.4}$$

Source evolution effects were not included in the benchmark scenario, and neither were the effects of magnetic fields. All the simulations were one-dimensional. With all these simplifications the total scenario included 7 independent parameters: spectral index, maximum rigidity, normalisation of the spectrum and 4 mass fraction values.

Next came the statistical methods of fitting the results of the simulations to the experimental data to derive the fitting parameters. The likelihood scanning happened as follows: a uniform scan over different combinations of the values of two parameters (spectral index and maximum rigidity) was done, and then for each pair the deviation from $X_{\max}$ distributions was minimized as a function of the fractions f_A. In the posterior sampling method a fit simultaneously constraining 6 main parameters (spectral index, maximum rigidity and 4 mass fractions) was applied, with Bayesian formalism (specifically Gelman-Ruben convergence diagnostics) used to deal with posterior probabilities sampled using a Markov chain Monte Carlo algorithm.

More details on the fitting procedure, the uncertainties and the results are given in the original paper of the combined fit [82].

The resulting parameters received in the combined fit can be implemented then into the simulations to make a prediction of the UHE photon flux we are interested in. However, it is not necessary for us to keep all the assumptions on the benchmark scenario that were used in the combined fit (e.g. the absence of a magnetic field), since these parameters can possibly have a significant impact on the associated photon flux. The results of these simulations are shown in Sec. 5.2.3.

5.2.2 Parameters study

Results of the combined fit presented in [82] specify most of the parameters of the propagation scenarios, yet the initial scenario of the propagation of UHECR used there is over-simplified (no magnetic field, no source evolution with redshift, etc). In order to make more trustworthy predictions of the UHE photon flux, one could include the magnetic field and source evolution with redshift, and discuss sources and photon background. In order to estimate the influence of these parameters on the UHE photon flux, quick parameter check is done in this section.

The '2nd minimum' parameters from the likelihood scanning are used as the benchmark scenario in this study. This parameter set is chosen for its spectral index and maximum rigidity values, as they are close to the ones of pure proton propagation scenarios presented in Ch. 4, so it would be easier to compare the results and estimate the difference.

The impact of the source redshift evolution is the same as for the pure proton cosmic rays: the steeper the evolution, the lower the UHE photon flux, see Fig. 5.2.1. UHE photon flux from sources with SFR type of evolution (m = 3.4) is nearly two times higher than the one from sources with QS type of evolution (m = 5.5) and nearly two times lower than the one from sources distributed uniformly (m = 0). For further propagation the evolution following star formation rate is chosen, m = 3.4. Magnetic field also influence the UHE photon flux in the

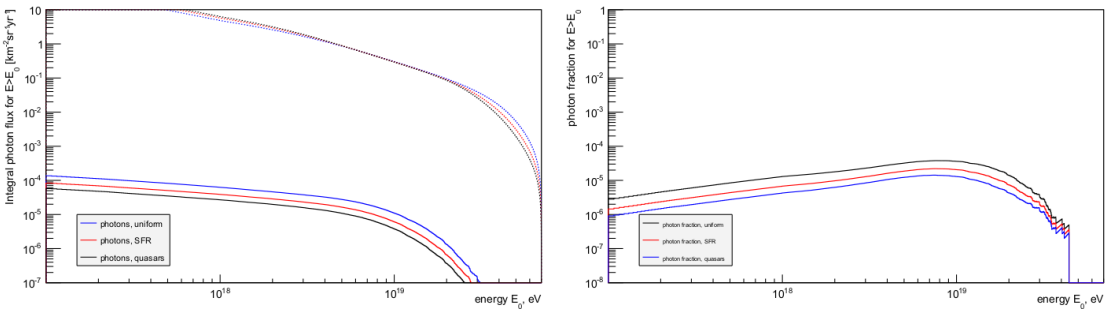

Figure 5.2.1: Impact of the source evolution with redshift on the UHE photon flux. *Left:* Integral photon fluxes (with total CR fluxes in dashed lines) in dependency of the threshold energy E_0. *Right:* Integral UHE photon fraction in dependency of the threshold energy E_0.

same way it does for the pure proton cosmic rays (Fig. 5.2.2). It is noticeable, however, that general absence or presence of the magnetic field has less impact on the UHE photon flux than in the case of pure pronot cosmic rays. The difference between the cases of no magnetic field and 1 nG is less notable in the current study. The magnetic field of 1 nG is used in further propagation. The universal radio background has no influence on the photon flux at all: photo-

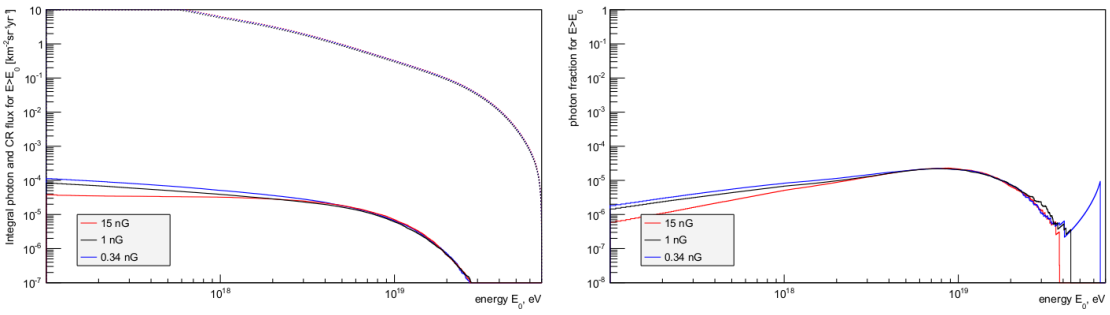

Figure 5.2.2: Impact of the magnetic field on the UHE photon flux. *Left:* Integral photon fluxes (with total CR fluxes in dashed lines) in dependency of the threshold energy E_0. *Right:* Integral UHE photon fraction in dependency of the threshold energy E_0.

nuclear processes are not determined on this background, and with heavier initial nuclei they dominate over EM cascade even more than for the pure proton CRs, so the effect of the URB disappears, see Fig. 5.2.3.

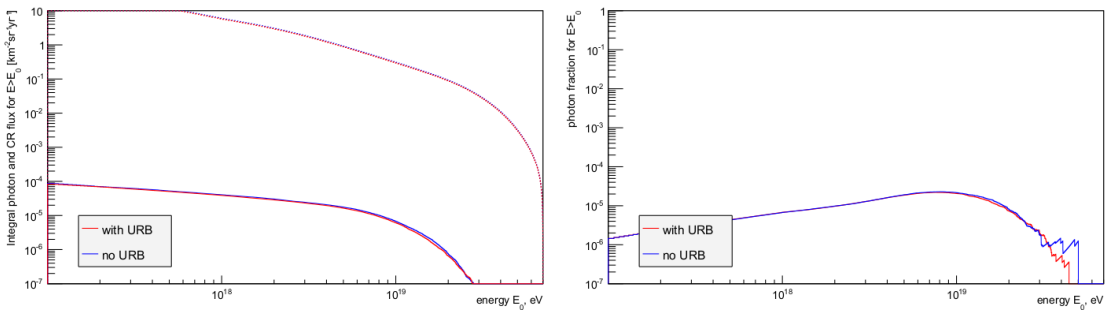

Figure 5.2.3: Impact of the presence of the universal radio background on the UHE photon flux. *Left:* Integral photon fluxes (with total CR fluxes in dashed lines) in dependency of the threshold energy E_0. *Right:* Integral UHE photon fraction in dependency of the threshold energy E_0.

5.2.3 Results

All three parameter sets from the results of the combined fit from [82] together with small improvements on the propagation scenario from the previous section are now plugged into the simulation to predict the UHE photon flux from these mixed initial cosmic rays.

The results of including the uncertainties on the values of parameters mentioned in Table 2 into the integral UHE photon fluxes for the main minimum (likelihood scanning) scenario are given in Fig. 5.2.4. 'Minimum' and 'maximum' scenarios for this study are derived to produce minimal and maximal UHE photon flux, with impact of the spectral index, maximum rigidity and composition fractions taken into account. Parameter are given in Table 3. From the Table 2, errors and intervals are larger for the mass fractions than the uncertainties on the spectral index and rigidity, and the latter have more notable impact on the propagation results. This is why the difference between the resulting fluxes is noticeable almost only for threshold energies $E_0 > 40$ EeV.

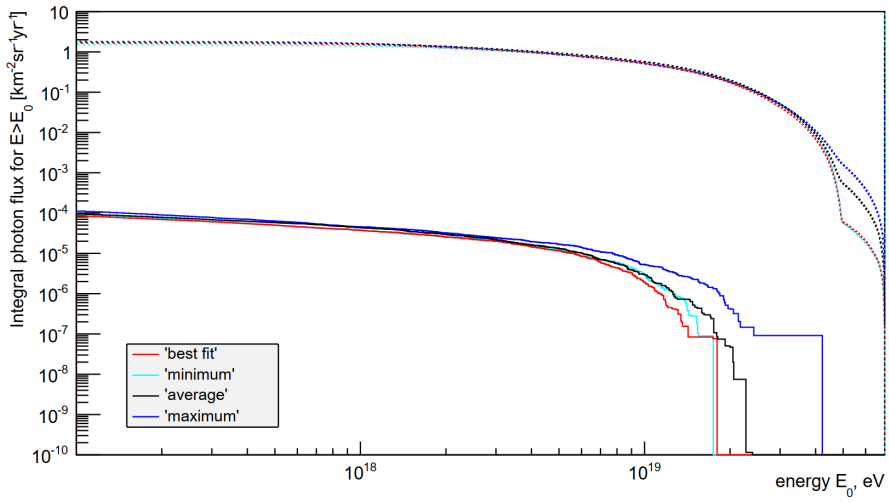

Figure 5.2.4: Integral photon fluxes (with total CR fluxes in dashed lines) in dependency of the threshold energy E_0. The parameters for the main minimum (LS) scenario are used for initial mixed CRs.

	best fit	average	minimum	maximum
α	0.96	0.93	1.05	0.81
$\log_{10}(R_{\text{cut-off}}/eV)$	18.68	18.66	18.62	18.70
$f_{\text{H}}(\%)$	0	12.5	0	31.7
$f_{\text{He}}(\%)$	67.3	58.6	61.0	49.9
$f_{\text{N}}(\%)$	28.1	24.6	33.5	15.5
$f_{\text{Si}}(\%)$	4.6	4.2	5.5	2.9

Table 3: Parameters of the propagation scenarios used in the study of the impact the uncertainties on the parameters derived in a fitting procedure have on the UHE photon flux. Parameters derived in [82] for the main minimum (LS) are used.

Gaps between the UHE photon fluxes shown in Fig. 5.2.4 represent the uncertainties on the flux that are only coming from the uncertainties on the parameters derived in a fitting procedure.

All three scenarios from Table 2 are presented in the Fig. 5.2.5. Blue lines represent the scenarios obtained by the likelihood scanning, and the red one is for the result of the posterior sampling. These three possible scenarios of the mixed UHECR propagation are obtained from the same data set, so the difference between the highest and the lowest UHE photon fluxes calculated with these scenarios can be treated as an estimation of all the uncertainties coming from choosing one or another result of the fitting procedure.

From comparing the lines, some features of the UHE photon flux produced by mixed cosmic rays are clear. Mass compositions are almost alike for main minimum (LS) and best fit (PS) scenarios, and so are the maximum rigidity values, so the difference between these lines originates mainly in the difference between the spectral indices (0.96 in main minimum (LS) and 1.22 in best fit (PS)). Main and 2nd minima (LS) scenarios lead to almost the same UHE photon fluxes for energy up to 1 EeV. UHE photon flux from the 2nd minimum is less steep due to much higher maximum rigidity. The significant difference between the compositions of main and 2nd minima (LS) scenarios results in the photo-disintegration kink in the total CR flux happening at lower energies for the main minimum scenario. These kinks also appear in the total CR flux of the two other scenarios, 2nd minimum (LS) and best fit (PS), only for higher energies, so they could not be observed in the plot.

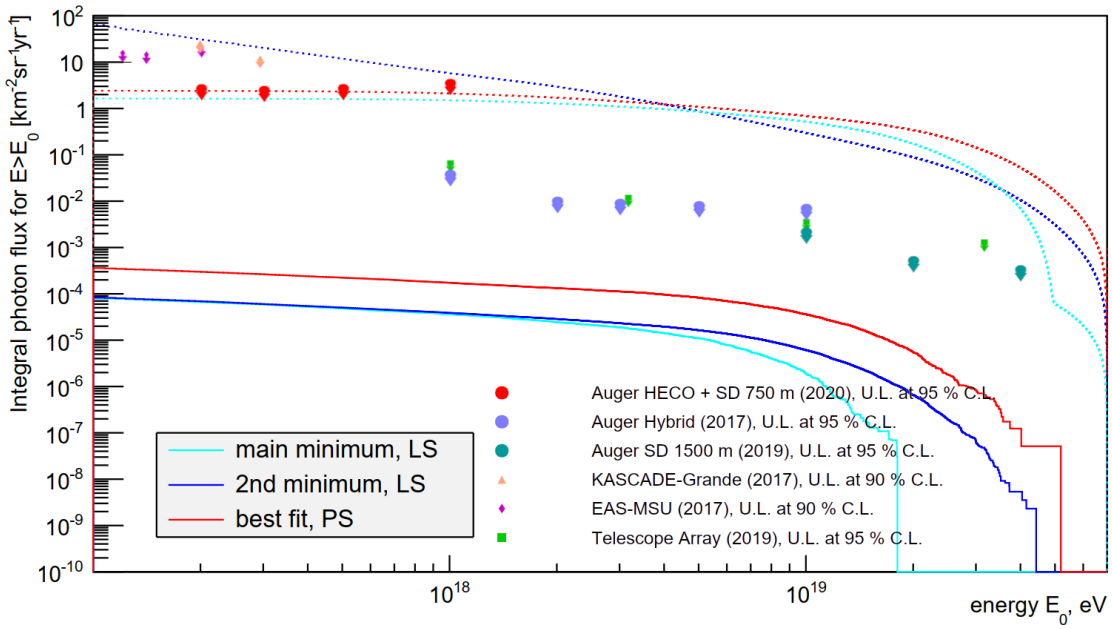

Figure 5.2.5: Prediction of the UHE photon flux from mixes cosmic ray propagation. Integral photon and total CR fluxes in dependency of the threshold energy E_0. Parameters of the propagation scenarios obtained by likelihood scanning (LS) and posterior sampling (PS) in [82] are used. Limits are the same as in Fig. 4.3.2.

Results of this study for mixed initial cosmic ray composition cannot be compared directly to the ones of pure proton and iron propagation (Fig. 4.3.2), as the combinations of spectral indices and maximum rigidity values are way too different. Therefore, the difference in composition is less important. It is safe to state that, with current propagation scenarios, the prediction of the UHE photon flux is higher for 'best fit, PS' in composition study than the one from pure proton propagation. This is due to the harder CR spectrum at the sources in the mixed composition case. However, is is noticeable that the predictions of the UHE photon flux from all these scenarios

are lower than the upper limits derived from experimental data.

6 Photon cosmic rays

In the previous chapters, UHE photons are considered as secondary messengers created during the cosmic ray propagation, yet they also could be initially emitted from the sources, as accelerated CR particles are capable of interacting within the source and produce UHE photons. Thus, these photons may contribute to the UHE photon flux on Earth. The study of the propagation of UHE photons is presented in this chapter. We look at a single UHE photon source with determined energy spectrum. As photons are not deflected in the magnetic field and could be propagated linearly, we perform a 1D propagation. We observe the number of photons that reach the detector placed at different distances from the source.

We are not looking at any specific source in this study, very general assumptions are made concerning the CR spectrum at the source. This procedure is a way to study the photon flux coming from any source, and with specific features taken into account this method can be developed into the study of different types of sources, for instance, neutron star mergers.

6.1 Attenuation length of the UHE photons

In order to describe the probability of the amount of photons to interact with matter, the parameter of attenuation length can be introduced. Attenuation length is the distance λ at which, if there were N initial photons, only N/e remain non-interacted. In current sub-chapter the study of the attenuation length of the UHE photons and its dependency on the energy of a photon is performed.

The scenario for this propagation is rather simple compared to the hadronic CR propagation, as all the photo-hadronic interactions and magnetic fields are skipped here. 5×10^5 initial photons are emitted, and only two interactions, pair production and double pair production, are included into propagation. As we are only interested in the distance that UHE photon travels before interacting, no secondary particles are taken into account. In case of pure photon propagation, no other interactions are considered, and the influence of the magnetic field can be neglected. All three main types of photon background (cosmic microwave background, infrared background light and universal radio background) are included. The study is performed for energy values in the range from 0.1 EeV to 100 ZeV (= 10^{21} eV). The procedure of the measurement happens as follows: for each energy value the propagation is done approximately 20 times with the source being moved increasingly farther away from the observer. The dependency of the number of photons left at a distance d from the source on the distance from the source is then fit with the exponential decay formula

$$N(d, E) = N_0 e^{-d/\lambda_{\text{int}}(E)} \tag{6.1}$$

where N is the number of particles reached the detector, N_0 is the initial number of photons, and λ_{int} is the interaction length of the particle, the mean free path between two interactions (or between the creation of a particle and its first interaction). The fitting procedure for one energy value (60 EeV) is shown in Fig. 6.1.1. Then, knowing the interaction length, the distances corresponding to percentage of remaining particles of $1\%, 5\%, 20\%$ and 36.8% are calculated, the latter being the attenuation length. The results are shown in Fig. 6.1.2. The values of distances, at which certain percentage of photons remains non-interacted, is given in Table 4. The results

shown in Fig. 6.1.2 reproduce the ones presented in Fig. 5.1 in [59].

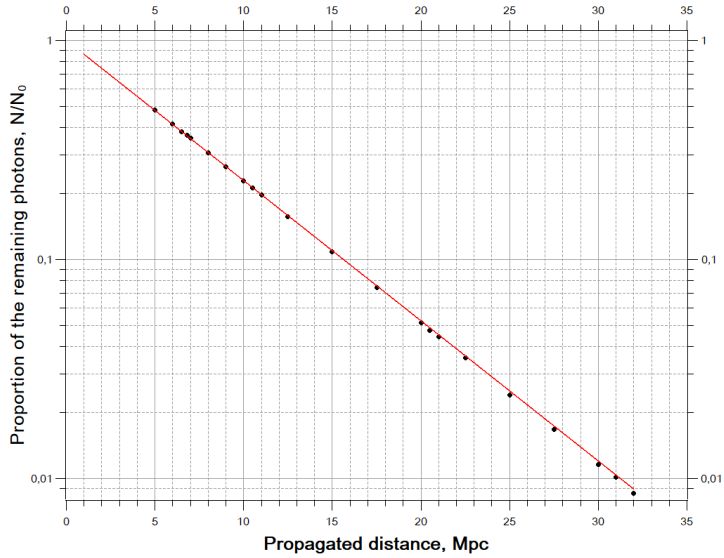

Figure 6.1.1: Proportion of the remaining photons as a function of the propagated distance. Red line is the fit with the function from Eq. 6.1. Energy of the photons is 60 EeV in this case.

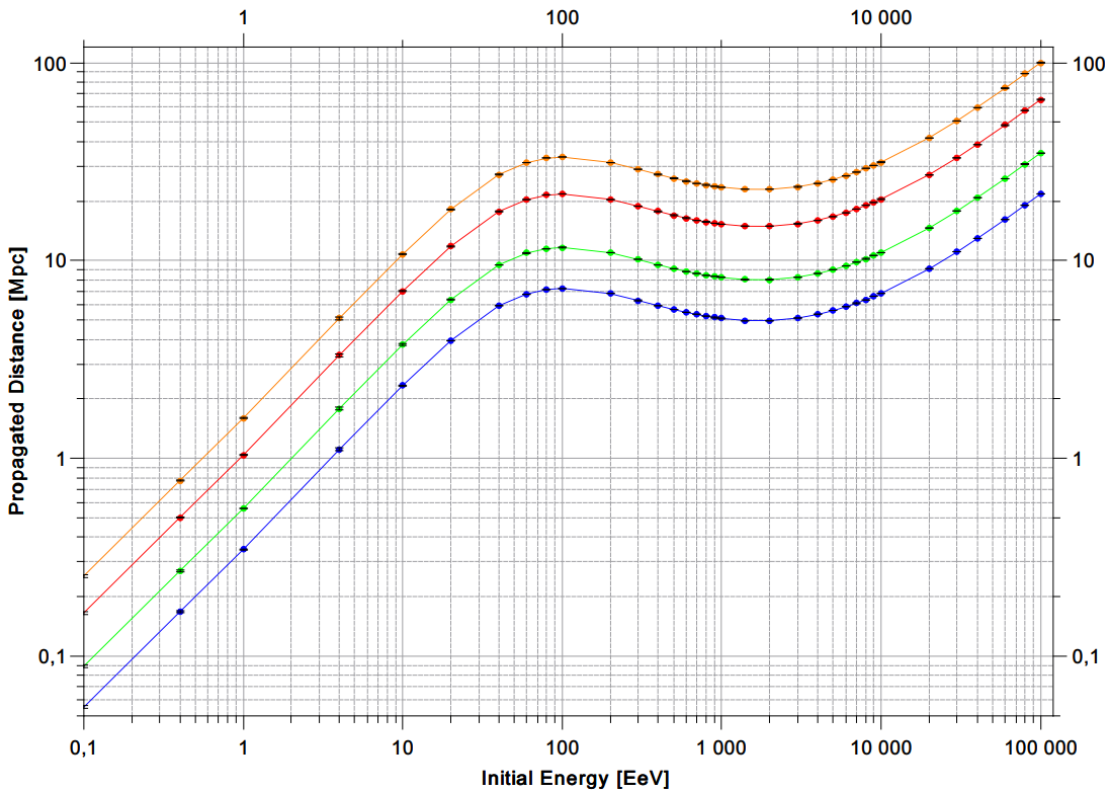

Figure 6.1.2: Distances at which a certain fraction of photons that have not interacted yet, as a function of the energy of photons. Orange dots correspond to 1% photons remained, red dotes — to 5%, green ones — to 20%, and the blue dots are marking the attenuation length (36.8%). Lines are linear interpolations between the calculated points.

Distances at which a certain fraction of remaining photons								
E, EeV	λ_{att}(36.8%)	$\pm\, d\lambda_{att}$, Mpc	λ(20%)	$\pm\, d\lambda$, Mpc	λ(5%)	$\pm\, d\lambda$, Mpc	λ(1%)	$\pm\, d\lambda$, Mpc
0.1	0.06	±0.001	0.09	±0.001	0.17	±0.003	0.26	±0.004
0.4	0.17	±0.001	0.27	±0.002	0.50	±0.004	0.77	±0.006
1	0.35	±0.002	0.56	±0.002	1.04	±0.004	1.60	±0.007
4	1.10	±0.003	1.77	±0.004	3.29	±0.007	5.06	±0.012
10	2.34	±0.02	3.76	±0.03	7.01	±0.05	10.77	±0.08
20	3.94	±0.02	6.34	±0.03	11.80	±0.05	18.14	±0.08
40	5.94	±0.08	9.55	±0.13	17.78	±0.24	27.33	±0.37
60	6.86	±0.19	11.04	±0.30	20.55	±0.56	31.59	±0.86
80	7.22	±0.17	11.61	±0.27	21.61	±0.50	33.23	±0.76
100	7.32	±0.17	11.78	±0.28	21.93	±0.52	33.71	±0.80
200	6.90	±0.21	11.10	±0.33	20.67	±0.62	31.77	±0.95
300	6.39	±0.21	10.28	±0.34	19.13	±0.63	29.41	±0.97
400	6.03	±0.22	9.71	±0.35	18.07	±0.65	27.77	±0.99
500	5.78	±0.22	9.30	±0.35	17.31	±0.66	26.60	±1.01
600	5.60	±0.21	9.02	±0.35	16.78	±0.64	25.80	±0.99
700	5.47	±0.22	8.81	±0.36	16.40	±0.67	25.20	±1.03
800	5.37	±0.23	8.64	±0.36	16.08	±0.67	24.73	±1.04
900	5.30	±0.23	8.53	±0.36	15.87	±0.68	24.40	±1.04
1000	5.25	±0.23	8.44	±0.37	15.72	±0.68	24.16	±1.05
1400	5.13	±0.23	8.25	±0.37	15.36	±0.69	23.62	±1.06
2000	5.12	±0.23	8.24	±0.37	15.34	±0.69	23.59	±1.06
3000	5.27	±0.23	8.47	±0.37	15.77	±0.68	24.25	±1.05
4000	5.47	±0.22	8.81	±0.36	16.40	±0.67	25.21	±1.03
5000	5.71	±0.22	9.19	±0.35	17.10	±0.66	26.28	±1.01
6000	5.95	±0.22	9.57	±0.35	17.82	±0.65	27.40	±1.00
7000	6.19	±0.21	9.97	±0.34	18.56	±0.64	28.53	±0.98
8000	6.44	±0.21	10.37	±0.34	19.30	±0.63	29.67	±0.97
9000	6.68	±0.21	10.75	±0.34	20.02	±0.62	30.77	±0.96
10000	6.91	±0.21	11.13	±0.33	20.71	±0.62	31.83	±0.95
20000	9.20	±0.29	14.80	±0.46	27.55	±0.86	42.35	±1.32
30000	11.15	±0.26	17.94	±0.42	33.39	±0.78	51.33	±1.20
40000	12.97	±0.25	20.88	±0.40	38.86	±0.74	59.74	±.13
60000	16.22	±0.31	26.10	±0.50	48.58	±0.93	74.69	±1.43
80000	19.13	±0.30	30.79	±0.48	57.32	±0.89	88.11	±1.38
100000	21.74	±0.29	34.99	±0.47	65.13	±0.87	100.13	±1.34

Table 4: Distances at which a certain fraction of photons have not interacted yet for different photon energy values. Uncertainties come from the fitting procedure and are due to statistical limitations.

.

6.2 Effective attenuation length

The knowledge of the attenuation length of the UHE photons is applicable to predicting the number of UHE photons at a detector on Earth that may come from specific objects or events in space. For instance, GW170817 event, the binary neutron star merger at a distance of ~ 40 Mpc

[85], can be studied. One can determine the upper limit on the total amount of energy emitted from the source in the form of UHE photons and then calculate the expected number of those reaching the detector. We perform such a study for the Pierre Auger Observatory surface detector (Auger SD, aperture $\approx$ 2400 km^2) and some model amounts of energy emitted in the form of UHE photons (from 10^{-7} $M_\odot$ to 10 $M_\odot$). It is assumed that the source is emitting UHE photons with a power law energy spectrum proportional to E^{-2} in the range from 10^{19} eV to $10^{20.5}$ eV, energy range of the photon search with the Auger SD which has been adopted for the search for photons from GW sources [67] [85]. Photons are propagated with the same scenario as in Sec. 6.1: no secondary particles, only UHE photons interacting with photon background via pair production or double pair production. The results are presented in Fig. 6.2.1.

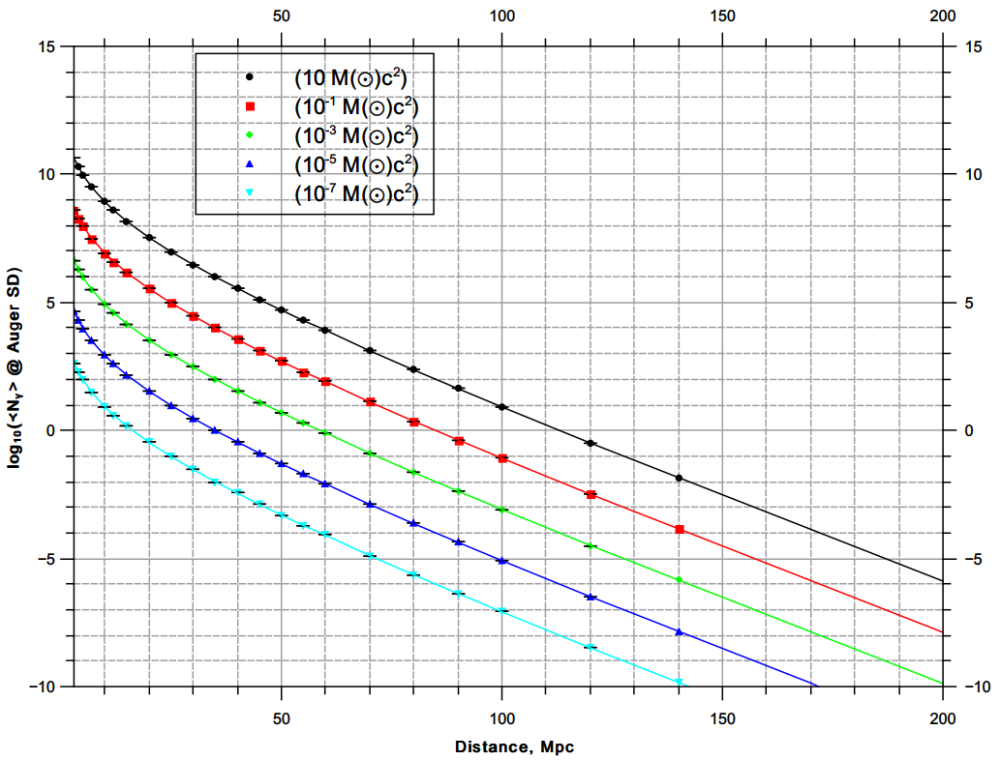

Figure 6.2.1: Total number of photons at Auger SD as a function of distance from the source for different amount of energy emitted in a form of UHE photons. Lines are cubic interpolations between the calculated points. Errors are calculated as binomial confidence intervals (95%).

This result is an update on the previous work presented in Fig. 8.10 in [85], where the same analysis of the total number of photons at Auger SD as a function of the distance from the source was made analytically with photons being assumed to be attenuated with an interaction length of 7 Mpc independent of their energy). With CRPropa 3 simulations there is no need for such an assumption, as the interaction length of a propagated particle is defined based on the properties of the particle (in this case, energy) at each propagation step. It can be noticed that the number of photons at Auger SD obtained in current research shown in Fig. 6.2.1 is about 5% higher than the previous ones, yet the general slope is almost the same.

As photons are not losing energy during the propagation, the assumption for a photon to have a constant interaction length at each step is reasonable, yet within the photon energies in a range from 10^{19} eV to $10^{20.5}$ eV the attenuation length of UHE photons is changing significantly (see

Fig. 6.1.2). If the effective attenuation length could be determined, then the number of UHE photons observed at the detector could be calculated analytically:

$$\langle N_\gamma(D)\rangle \propto E_{\text{tot}} \exp(-D/\lambda_{\text{eff}}) \frac{2400\,\text{km}^2}{4\pi D^2} \tag{6.2}$$

where D is the distance from the source, E_{tot} is the initial amount of energy emitted in the form of UHE photons, λ_{eff} is the effective attenuation length and all the parameters of the translation from an amount of energy to the number of UHE photons are included into the constant of proportion.

In order to determine the effective attenuation length the attempt to fit the results from Fig. 6.2.1 with the function shown in Eq. 6.2 is performed. It appeared, however, that it is not possible to find one effective attenuation length for all the distance ranges: in Fig. 6.2.2 five attempts with different distance ranges of fitting are shown. None of the functions describe the total dependency. Values of the derived effective attenuation length are presented in Table 5.

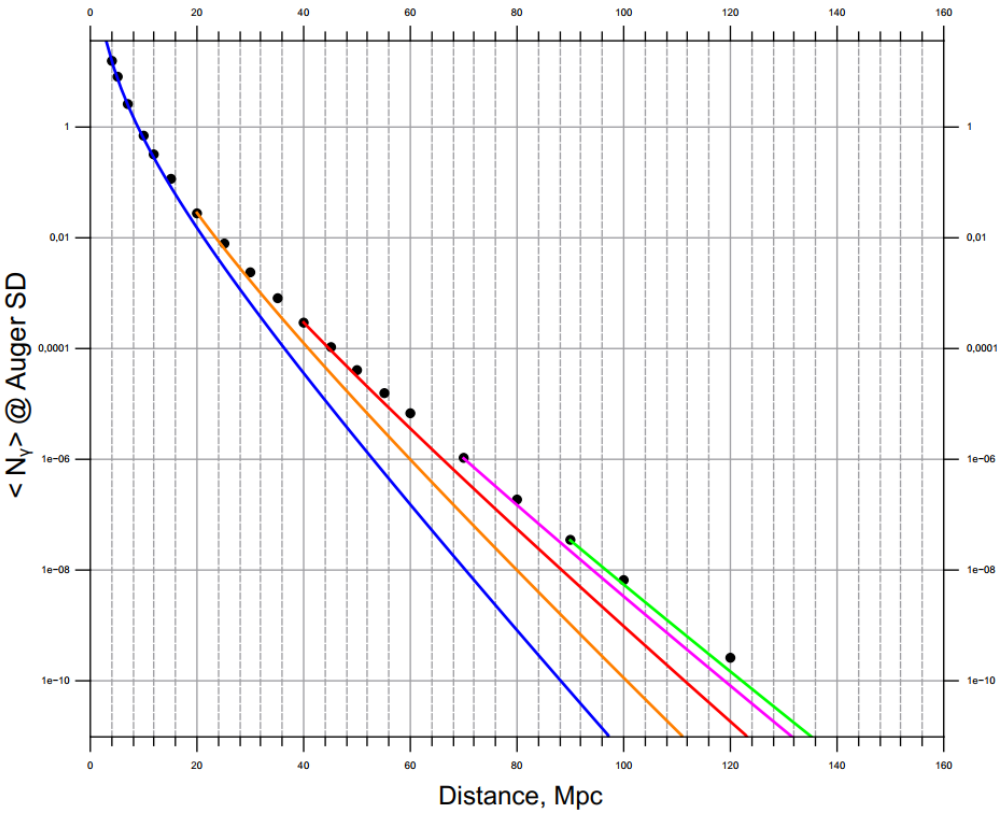

Figure 6.2.2: Attempts to fit the dependency of total number of photons at Auger SD on distance from the source. Blue line is the fitting curve for data in distance range from 3 Mpc to 140 Mpc, orange line - from 20 Mpc to 140 Mpc, red line - from 40 Mpc to 140 Mpc, purple line - from 70 Mpc to 140 Mpc, green line - from 90 Mpc to 140 Mpc.

It can be noticed that the effective attenuation length is increasing with the minimum of the distance range included in the fitting. As we know from Fig. 6.1.2, the attenuation length of a photon in the energy range from 10^{19} eV to $10^{20.5}$ eV increases (from 2.34 Mpc to 7.32 Mpc) with the energy of the UHE photon up to 10^{20} eV and then slightly decreases (from 7.32 Mpc

D_{min}, Mpc	λ_{eff}, Mpc
3	4.31
20	4.98
40	5.57
70	5.98
90	6.16

Table 5: Effective attenuation length determined from fitting the data in the distance range from D_{min} to 140 Mpc

.

to approximately 6.3 Mpc) up to $10^{20.5}$ eV. This means that for larger distances only photons of energies around 10^{20} eV may avoid interaction. Also, the effective attenuation length at larger distances is expected to converge to the value of 7.32 Mpc, the maximum attenuation length in current energy region. This we do not see with fitting, but it can probably be achieved with increasing the distance range. For this study, the increase of initial number of photons is required.

As a result of the study, including the energy dependence of the photon attenuation length could help to improve photon predictions from nearby sources.

7 Summary and outlook

Within the scope of this thesis propagation of the hadronic UHECR is performed for different astrophysical scenarios. New predictions for the UHE photon flux from GZK-interactions of hadronic cosmic rays are derived.

Predictions of the UHE photon flux from the pure proton cosmic rays have been compared to previous predictions derived in [8]. Parameters of the propagation scenario used in that research are different from the ones of the current thesis, and with the maximum rigidity being an order of magnitude higher in [8] it is no surprise to have the predictions of several orders of magnitude higher for UHE photon flux. If comparing to predictions made in [9], where astrophysical scenarios for pure proton initial cosmic rays are the same as in current thesis, the results are very much alike, except for minor distinctions probably coming from different versions of CRPropa framework.

Predictions of the UHE photon flux from mixed cosmic rays appeared to be mostly dependent on the parameters of the energy spectrum of CR at the source and the fraction of protons in the initial composition. Photo-disintegration, the main photo-hadronic interaction for nuclei heavier than the proton, reduces the impact of the mass of the initial nuclei on the UHE photon flux on Earth.

For both pure proton and mixed compositions the predictions stay below the upper limits on the UHE photon flux on Earth derived from the experimental data. Main uncertainties on the predictions are coming from not yet full understanding of the UHECR sources and their features.

Ultra high energy photons could not only be produced in the interactions of UHECR with photon background, but also be created at the sources themselves. Correlation between the power and distance of the source and the photon flux on Earth coming from that source is described. Comparing to [85], the less simplifications are made, as the energy dependence of the photon attenuation length is taken into account.

With more and more data being observed at the Pierre Auger Observatory and other experiments more precise results will be obtained in the future on the spectrum and the composition of the UHECR, and the methods developed in this thesis could be then used again to give new predictions of the UHE photon flux on Earth. With more information on the sources of the UHECR (e.g. their distribution and anisotropy), more specific predictions could be calculated in the future. For the photon propagation study, less simplification could be used in the research. For specific sources like GW170817, more precise photon predictions could be made by including models of galactic and extragalactic magnetic fields and using 3D propagation. This way, also the relevance of secondary photons from GW170817 could be investigated.

References

1. Aab, A. *et al.* The Pierre Auger Cosmic Ray Observatory. *Nuclear Instruments and Methods in Physics Research Section A: Accelerators, Spectrometers, Detectors and Associated Equipment* **798,** 172–213 (2015).
2. Greisen, K. End to the Cosmic-Ray Spectrum? *Phys. Rev. Lett.* **16,** 748–750 (17 Apr. 1966).
3. Zatsepin, G. T. & Kuz'min, V. A. Upper Limit of the Spectrum of Cosmic Rays. *Soviet Journal of Experimental and Theoretical Physics Letters* **4,** 78 (Aug. 1966).
4. Apel, W. D. *et al.* KASCADE-Grande Limits on the Isotropic Diffuse Gamma-Ray Flux between 100 TeV and 1 EeV. *The Astrophysical Journal* **848,** 1 (Oct. 2017).
5. Abbasi, R. *et al.* Constraints on the diffuse photon flux with energies above 10^{18} eV using the surface detector of the Telescope Array experiment. *Astroparticle Physics* **110,** 8–14 (July 2019).
6. Fomin, Y. A. *et al.* Constraints on the flux of $\sim (10^{16} - 10^{17.5})$ eV cosmic photons from the EAS–MSU muon data. *Phys. Rev. D* **95,** 123011 (12 June 2017).
7. Gelmini, G., Kalashev, O. & Semikoz, D. GZK photons as ultra-high-energy cosmic rays. *J. Exp. Theor. Phys.* **106,** 1061 (2008).
8. Sarkar, B., Kampert, K.-H. & Kulbartz, J. Ultra-High Energy Photon and Neutrino Fluxes in Realistic Astrophysical Scenarios. *32nd International Cosmic Ray Conference* **2,** 198 (2011).
9. Sarkar, B. *Constraints to UHE cosmic ray source scenarios with all the major observables of the Pierre Auger Observatory* PhD thesis (Sept. 2015).
10. Aab, A. *et al.* Depth of maximum of air-shower profiles at the Pierre Auger Observatory. I. Measurements at energies above$10^{17.8}$eV. *Physical Review D* **90** (Dec. 2014).
11. Aab, A. *et al.* Depth of maximum of air-shower profiles at the Pierre Auger Observatory. II. Composition implications. *Phys. Rev. D* **90** (12 Dec. 2014).
12. Aab, A. *et al.* Interpretation of the depths of maximum of extensive air showers measured by the Pierre Auger Observatory. *Journal of Cosmology and Astroparticle Physics* **2013,** 026–026 (Feb. 2013).
13. Gaisser, T. K., Engel, R. & Resconi, E. *Cosmic Rays and Particle Physics* 2nd ed. (Cambridge University Press, 2016).
14. Hess, V. F. Über Beobachtungen der durchdringenden Strahlung bei sieben Freiballonfahrten. (English Translation). *Physikalische Zeitschrift* **13,** 1084–1091 (1912).
15. Kolhörster, W. Messungen der durchdringenden Strahlungen bis in Höhen von 9300 m. *Verh. Dtsch. Phys. Ges* **16,** 719–721 (1914).
16. Evoli, C. *The Cosmic Ray Energy Spectrum* https://doi.org/10.5281/zenodo.2360277. (accessed: 15.09.2020).
17. Murzin, V. *Astrophysics of the Cosmic Rays (Russian)* (Logos, 2007).
18. Letessier-Selvon, A. & Stanev, T. Ultrahigh energy cosmic rays. *Rev. Mod. Phys.* **83,** 907–942 (Sept. 2011).

19. Apel, W. D. *et al.* Kneelike Structure in the Spectrum of the Heavy Component of Cosmic Rays Observed with KASCADE-Grande. *Phys. Rev. Lett.* **107,** 171104 (Oct. 2011).
20. Olive, K. Review of Particle Physics. *Chinese Physics C* **38,** 090001 (Aug. 2014).
21. Mollerach, S. & Roulet, E. Progress in high-energy cosmic ray physics. *Progress in Particle and Nuclear Physics* **98,** 85–118 (Jan. 2018).
22. Aguilar, M. *et al.* Precision Measurement of the Proton Flux in Primary Cosmic Rays from Rigidity 1 GV to 1.8 TV with the Alpha Magnetic Spectrometer on the International Space Station. *Phys. Rev. Lett.* **114,** 171103 (17 Apr. 2015).
23. Aguilar, M. *et al.* Precision Measurement of the Helium Flux in Primary Cosmic Rays of Rigidities 1.9 GV to 3 TV with the Alpha Magnetic Spectrometer on the International Space Station. *Phys. Rev. Lett.* **115,** 211101 (21 Nov. 2015).
24. Engelmann, J. J. *et al.* Charge composition and energy spectra of cosmic-ray nuclei for elements from Be to Ni - Results from HEAO-3-C2. **233,** 96–111 (July 1990).
25. Yoon, Y. S. *et al.* Proton and Helium Spectra from the CREAM-III Flight. *The Astrophysical Journal* **839,** 5 (Apr. 2017).
26. Ahn, H. S. *et al.* Energy spectra of cosmic ray nuclei at high energies. *The Astrophysical Journal* **707,** 593–603 (Nov. 2009).
27. Apel, W. *et al.* Energy spectra of elemental groups of cosmic rays: Update on the KASCADE unfolding analysis. *Astroparticle Physics* **31,** 86–91 (Mar. 2009).
28. Apel, W. *et al.* KASCADE-Grande measurements of energy spectra for elemental groups of cosmic rays. *Astropart. Phys.* **47,** 54–66 (2013).
29. Pérez-Peraza, J. A. & Libin, I. Y. *Highlights in Helioclimatology* (Elsevier, 2012).
30. Risse, M. & Homola, P. Search for Ultra-High energy photons using air showers. *Modern Physics Letters A* **22,** 749–766 (Apr. 2007).
31. Ostrowski, M. *Cosmic ray acceleration at relativistic shocks, shear layers* 2008.
32. Fermi, E. On the Origin of the Cosmic Radiation. *Phys. Rev.* **75,** 1169–1174 (Apr. 1949).
33. Viganò, D., Torres, D. F., Hirotani, K. & Pessah, M. E. Compact formulae, dynamics and radiation of charged particles under synchro-curvature losses. *Monthly Notices of the Royal Astronomical Society* **447,** 1164–1172 (Dec. 2014).
34. Hillas, A. M. The Origin of Ultra-High-Energy Cosmic Rays. *Annual Review of Astronomy and Astrophysics* **22,** 425–444 (1984).
35. Ptitsyna, K. V. & Troitsky, S. V. Physical conditions in potential accelerators of ultra-high-energy cosmic rays: updated Hillas plot and radiation-loss constraints. *Uspekhi Fizicheskikh Nauk (UFN)* **53,** 691–701 (Oct. 2010).
36. Alves Batista, R. *et al.* Open Questions in Cosmic-Ray Research at Ultrahigh Energies. *Frontiers in Astronomy and Space Sciences* **6** (June 2019).
37. Ginzburg, V. & Syrovatskii, S. *The Origin of the Cosmic Rays* (Pergamon, 1964).
38. Ackermann M, e. a. Detection of the Characteristic Pion-Decay Signature in Supernova Remnants. *Science* **339,** 807–811 (Feb. 2013).
39. Michel, F. Cosmic-ray acceleration by pulsars. *Advances in Space Research* **4,** 387–391 (1984).

40. Blasi, P., Epstein, R. I. & Olinto, A. V. Ultra–High-Energy Cosmic Rays from Young Neutron Star Winds. *The Astrophysical Journal* **533,** L123–L126 (Apr. 2000).
41. Arons, J. Magnetars in the Metagalaxy: An Origin for Ultra–High-Energy Cosmic Rays in the Nearby Universe. *The Astrophysical Journal* **589,** 871–892 (June 2003).
42. Zackrisson, E. Quasars and Low Surface Brightness Galaxies as Probes of Dark Matter (May 2005).
43. Oort, J. H. The Galactic Center. *Annual Review of Astronomy and Astrophysics* **15,** 295–362 (1977).
44. Berezinsky, V., Gazizov, A. & Grigorieva, S. On astrophysical solution to ultrahigh energy cosmic rays. *Phys. Rev. D* **74,** 043005 (Aug. 2006).
45. Kennicutt, R. C. J. & Evans, N. J. I. *Star Formation in the Milky Way and Nearby Galaxies* 2012.
46. Anchordoqui, L. A., Romero, G. E. & Combi, J. A. Heavy nuclei at the end of the cosmic-ray spectrum? *Phys. Rev. D* **60,** 103001 (10 Oct. 1999).
47. Azzam, W. J., Zitouni, H. & Guessoum, N. Gamma-Ray Bursts: Characteristics and Prospects. *Journal of Physics: Conference Series* **869,** 012065 (June 2017).
48. Hopkins, A. M. & Beacom, J. F. On the Normalization of the Cosmic Star Formation History. **651,** 142–154 (Nov. 2006).
49. Yüksel, H., Kistler, M. D., Beacom, J. F. & Hopkins, A. M. Revealing the High-Redshift Star Formation Rate with Gamma-Ray Bursts. *The Astrophysical Journal* **683,** L5–L8 (July 2008).
50. Le, T. & Dermer, C. D. On the Redshift Distribution of Gamma-Ray Bursts in theSwiftEra. *The Astrophysical Journal* **661,** 394–415 (May 2007).
51. Kotera, K., Allard, D. & Olinto, A. Cosmogenic neutrinos: parameter space and detectabilty from PeV to ZeV. *Journal of Cosmology and Astroparticle Physics* **2010,** 013–013 (Oct. 2010).
52. Wall, J. V., Jackson, C. A., Shaver, P. A., Hook, I. M. & Kellermann, K. I. The Parkes quarter-Jansky flat-spectrum sample. *Astronomy Astrophysics* **434,** 133–148 (Apr. 2005).
53. Beck, R. Galactic and Extragalactic Magnetic Fields. *Space Science Reviews* **99,** 243–260 (Oct. 2001).
54. Haverkorn, M. Magnetic Fields in the Milky Way. *Magnetic Fields in Diffuse Media,* 483–506 (Oct. 2014).
55. Pshirkov, M. S., Tinyakov, P. G., Kronberg, P. P. & Newton-McGee, K. J. Deriving global structure of the Galactic Magnetic Field from Faraday Rotation Measures of extragalactic sources. *The Astrophysical Journal* **738,** 192 (Aug. 2011).
56. Jansson, R. & Farrar, G. R. A New Model of the Galactic Magnetic Field. *The Astrophysical Journal* **757,** 14 (Aug. 2012).
57. Dolag, K., Grasso, D., Springel, V. & Tkachev, I. Constrained simulations of the magnetic field in the local Universe and the propagation of ultrahigh energy cosmic rays. *Journal of Cosmology and Astroparticle Physics* **2005,** 009–009 (Jan. 2005).
58. Sigl, G., Miniati, F. & Enßlin, T. A. Ultrahigh energy cosmic ray probes of large scale structure and magnetic fields. *Physical Review D* **70** (Aug. 2004).

59. Heiter, C. *Production and Propagation of Ultra-High Energy Photons with CRPropa 3.0* Sept. 2016.

60. Protheroe, R. & Biermann, P. A new estimate of the extragalactic radio background and implications for ultra-high-energy γ-ray propagation. *Astroparticle Physics* **6,** 45–54 (Dec. 1996).

61. Gilmore, R. C., Somerville, R. S., Primack, J. R. & Domínguez, A. Semi-analytic modelling of the extragalactic background light and consequences for extragalactic gamma-ray spectra. *Monthly Notices of the Royal Astronomical Society* **422,** 3189–3207 (Apr. 2012).

62. Grieder, P. K. in *Extensive Air Showers: High Energy Phenomena and Astrophysical Aspects A Tutorial, Reference Manual and Data Book* 479–588 (Springer Berlin Heidelberg, Berlin, Heidelberg, 2010).

63. Khan, E. *et al.* Photodisintegration of ultra-high-energy cosmic rays revisited. *Astroparticle Physics* **23,** 191–201 (2005).

64. Allard, D. Extragalactic propagation of ultrahigh energy cosmic-rays. *Astropart. Phys.* **39-40,** 33–43 (2012).

65. Kelner, S. R. & Aharonian, F. A. Energy spectra of gamma rays, electrons, and neutrinos produced at interactions of relativistic protons with low energy radiation. *Phys. Rev. D* **78,** 034013 (3 Aug. 2008).

66. Batista, R. A., Boncioli, D., di Matteo, A., Vliet, A. v. & Walz, D. Effects of uncertainties in simulations of extragalactic UHECR propagation, using CRPropa and SimProp. *Journal of Cosmology and Astroparticle Physics* **2015,** 063–063 (Oct. 2015).

67. Rautenberg, J. Limits on ultra-high energy photons with the Pierre Auger Observatory. *PoS,* 398 (2019).

68. Amenomori, M. *et al.* First Detection of Photons with Energy beyond 100 TeV from an Astrophysical Source. *Physical Review Letters* **123** (July 2019).

69. Niechciol, M. Diffuse and targeted searches for ultra-high-energy photons using the hybrid detector of the Pierre Auger Observatory. *Proceedings of 35th International Cosmic Ray Conference — PoS(ICRC2017)* **301,** 517 (2017).

70. Batista, R. A. *et al.* CRPropa 3 — a public astrophysical simulation framework for propagating extraterrestrial ultra-high energy particles. *Journal of Cosmology and Astroparticle Physics* **2016,** 038–038 (May 2016).

71. Settimo, M. & De Domenico, M. Propagation of extragalactic photons at ultra-high energy with the EleCa code. *Astroparticle Physics* **62,** 92–99 (Mar. 2015).

72. Lee, S. Propagation of extragalactic high energy cosmic and γ rays. *Phys. Rev. D* **58,** 043004 (July 1998).

73. Tonry, J. L. *et al.* The SBF Survey of Galaxy Distances. IV. SBF Magnitudes, Colors, and Distances. *The Astrophysical Journal* **546,** 681–693 (Jan. 2001).

74. Castellina, A. Highlights from the Pierre Auger Observatory. *PoS,* 004 (2019).

75. Bergström, L. & Goobar, A. in *Cosmology and Particle Astrophysics* 59–87 (Springer Berlin Heidelberg, Berlin, Heidelberg, 2004).

76. Heiter, C., Kuempel, D., Walz, D. & Erdmann, M. Production and propagation of ultra-high energy photons using CRPropa 3. *Astroparticle Physics* **102,** 39–50 (Nov. 2018).

77. Bird, D. J. *et al.* Detection of a cosmic ray with measured energy well beyond the expected spectral cutoff due to cosmic microwave radiation. *The Astrophysical Journal* **441,** 144 (Mar. 1995).

78. Niechciol, M. & Risse, M. Search for primary photons with the hybrid detector at energies above 2×10^{17}eV: application to data, internal note GAP 2020-044 (2020).

79. Aab, A. *et al.* Erratum: Search for photons with energies above 10^{18}eV using the hybrid detector of the Pierre Auger Observatory. *Journal of Cosmology and Astroparticle Physics* **2020,** E02–E02 (Sept. 2020).

80. Kneiske, T. M., Bretz, T., Mannheim, K. & Hartmann, D. H. Implications of cosmological gamma-ray absorption. *Astronomy Astrophysics* **413,** 807–815 (Jan. 2004).

81. Schulz, A. The measurement of the energy spectrum of cosmic rays above 3x10$^{17} eV with the Pierre Auger Observatory. *33rd International Cosmic Ray Conference,* 769 (2013).

82. Aab, A. *et al.* Combined fit of spectrum and composition data as measured by the Pierre Auger Observatory. *Journal of Cosmology and Astroparticle Physics* **2017,** 038–038 (Apr. 2017).

83. Aloisio, R. Acceleration and propagation of ultra high energy cosmic rays. *Progress of Theoretical and Experimental Physics* **2017** (July 2017).

84. Domenico, M. D., Settimo, M., Riggi, S. & Bertin, E. Reinterpreting the development of extensive air showers initiated by nuclei and photons. *Journal of Cosmology and Astroparticle Physics* **2013,** 050–050 (July 2013).

85. Ruehl, P. *Probing the Sources of Gravitational Waves - A Search for UHE Photons Induced by Compact Binary Mergers at the Pierre Auger Observatory* PhD thesis (Sept. 2020).

Erklärung

Hiermit erkläre ich, dass ich die vorliegende Master-Arbeit selbständig verfasst und keine anderen als die angegebenen Quellen und Hilfsmittel benutzt, sowie Zitate und Ergebnisse Anderer kenntlich gemacht habe.

(Ort) (Datum) (Unterschrift)